1 **Cell-Cell Adhesion During Nephron Development Is Driven by Wnt/PCP Formin**
2 **Daam1**
3
4 Vanja Krneta-Stankic[1,2], Mark Corkins[2], Adriana Paulucci-Holthauzen[3], Malgorzata Kloc[3,4],

5 Andrew Gladden[1,3,5], Rachel Miller[1,2,3,6, *]

6
7 [1]MD Anderson Cancer Center UTHealth Graduate School of Biomedical Sciences, Program in
8 Genes and Development, Houston, TX, USA
9 [2]Department of Pediatrics, Pediatric Research Center, UTHealth McGovern Medical School,
10 Houston, TX, USA
11 [3]Department of Genetics, University of Texas MD Anderson Cancer Center, Houston, TX, USA
12 [4]Houston Methodist Hospital Research Institute, Houston, TX, USA
13 [5]Department of Pathology and Laboratory Medicine, University of North Carolina, Chapel Hill,
14 NC, USA
15 [6]MD Anderson Cancer Center UTHealth Graduate School of Biomedical Sciences, Program in
16 Biochemistry and Cell Biology, Houston, TX, USA
17 *Correspondence: Rachel.K.Miller@uth.tmc.edu
18

19 **SUMMARY**

20 E-cadherin junctions facilitate the assembly and disassembly of cell-cell contacts that drive

21 development and homeostasis of epithelial tissues. The stability of E-cadherin-based junctions

22 highly depends on their attachment to the actin cytoskeleton, but little is known about how the

23 assembly of junctional actin filaments is regulated. Formins are a conserved group of proteins

24 responsible for the formation and elongation of filamentous actin (F-actin). In this study, using

25 *Xenopus* embryonic kidney and Madin-Darby canine kidney (MDCK) cells, we investigate the

26 role of the Wnt/ planar cell polarity (PCP) formin protein Daam1 (Dishevelled-associated

27 activator of morphogenesis 1) in regulating E-cadherin based intercellular adhesion. Using live

28 imaging we show that Daam1 localizes to newly formed cell-cell contacts in the developing

29 nephron. Furthermore, analyses of junctional F-actin upon Daam1 depletion indicate a

30 decrease in microfilament localization and their slowed turnover. We also show that Daam1 is

31 necessary for efficient and timely localization of junctional E-cadherin, which is mediated by

32 Daam1's formin homology domain 2 (FH2). Finally, we establish that Daam1 signaling is

1

33   essential for promoting organized movement of renal cells. This study demonstrates that Daam1

34   formin junctional activity is critical for epithelial tissue organization.

35

36   **Keywords**

37   E-cadherin; F-actin; adhesion; kidney; nephron; Daam1; formin; Wnt; planar cell polarity;

38   *Xenopus*; collective cell movements; convergence and extension; tubulogenesis

39

40   **INTRODUCTION**

41   Extensive cellular rearrangements with changes in cell shape drive morphogenesis, including

42   for example, the process of tubulogenesis. To execute these processes successfully, cells must

43   be able to interact with each other and their environment in a timely and coordinated manner.

44   These interactions entail transduction of specific signals arising from adhesive contacts with the

45   extracellular matrix (ECM) and neighboring cells. How cells remodel their adhesions is one of

46   the central questions in epithelial tissue biology.

47

48   The cadherin family of cell adhesion proteins such as E-cadherin facilitate intercellular adhesion

49   and formation of cellular junctions (Adams et al., 1998; Takeichi, 2014; Yap et al., 2015).

50   Changes in E-cadherin-based adhesion are associated with developmental disorders and

51   progression of disease (Friedl and Mayor, 2017; Mendonsa et al., 2018). E-cadherin levels at

52   intercellular contacts depend on the organization of the actin cytoskeleton, but much remains to

53   be learned about how the actin assembly is regulated at these adhesive sites. Moreover, much

54   of our understanding of *in vivo* actin regulation and dynamics in cell-cell adhesion derives from

55   observations in cell culture systems, invertebrate embryos and the vertebrate skin.

56   Understanding of junction dynamics in intact vertebrae tissues is challenging, due to technical

57   limitations and tissue inaccessibility. In this study, we probe the role of the formin protein

58   Dishevelled-associated activator of morphogenesis 1 (Daam1) in intercellular adhesion during

2

59 kidney development using *Xenopus laevis* embryonic kidney and Madin-Darby canine kidney

60 (MDCK) cells.

61

62 Similar to many organs in our body, the kidney consists of a network of epithelial tubules. The

63 epithelial tubules of the kidney are called nephrons whose morphology is vital to kidney function.

64 Mesenchymal-epithelial transitions (MET) and coordinated cell rearrangements facilitate

65 nephron morphogenesis. Nephrons arise from the mass of mesenchymal cells that undergo

66 MET to form tubules consisting of tightly connected epithelial cells (McMahon, 2016; Saxen,

67 1987). Oriented cell intercalations drive the elongation of nephric tubules through a process

68 called convergent-extension (CE) (Castelli et al., 2013; Karner et al., 2009; Kunimoto et al.,

69 2017; Lienkamp et al., 2012). Extensive cytoskeletal rearrangements characterized by changes

70 in cell shape and coordinated cell movements accompany CE. Although E-cadherin-based

71 adhesions are implicated in mediating both MET and maintenance of coordinated cell

72 rearrangements (Campbell and Casanova, 2016), very little is known about how they function in

73 nephrogenesis (Combes et al., 2015; Lefevre et al., 2017; Marciano et al., 2011; Vestweber et

74 al., 1985).

75

76 Daam1 is a formin protein required for nephric tubulogenesis (Miller et al., 2011). Formin

77 proteins coordinate the organization of the actin cytoskeleton by nucleating and polymerizing

78 unbranched actin filaments. While Rho GTPases activate most formins, the activation of Daam1

79 depends on its interaction with Dishevelled (Dvl), a key intracellular component of the Wnt

80 signaling pathway (Liu et al., 2008). The Wnt signaling pathway plays important roles in nephron

81 development (McMahon, 2016; Miller and McCrea, 2009). The secreted Wnt ligands bind

82 Frizzled (Fz) receptors and subsequently, via Dvl regulate the canonical (β--catenin-dependent)

83 and non-canonical (β--catenin-independent)/planar cell polarity (PCP) signaling. While the

84 canonical signaling commonly governs inductive events and cell fate, the non-canonical/PCP

85   branch is associated with influencing cell behaviors and morphology. Nonetheless, the roles for

86   different branches of the Wnt pathway continue to evolve as recent studies provide evidence for

87   cross-talk between these two branches (Nagy et al., 2016; O'Brien et al., 2018). Dvl regulates

88   the non-canonical/PCP branch of the Wnt pathway through direct interaction with Daam1 (Liu et

89   al., 2008).

90

91   Increasing evidence suggests that formins may function as key regulators of the actin assembly

92   at the cell-cell junctions (Grikscheit and Grosse, 2016). Recent work in a mouse mammary

93   gland epithelial cell line, for example, has indicated that Daam1 is important for the stability of

94   epithelial cell junctions (Nishimura et al., 2016). Here, we expand on these findings by

95   examining the functional role of Daam1 in cellular junctions in the context of tissue

96   morphogenesis by analyzing its role in nephron development. Furthermore, using live cell

97   imaging we show that during establishment of cellular junctions, Daam1 first localizes to cellular

98   protrusions that initiate cell-cell contact, and subsequently, to newly formed junctions to promote

99   their stability. We find that Daam1 facilitates nephron morphogenesis by regulating the

100   assembly of junctional filamentous actin (F-actin) and in turn promotes the E-cadherin-based

101   epithelial adhesion.

102

103   **RESULTS**

104   **Daam1 co-localizes with F-actin and E-cadherin within the nephric primordium**

105   Knockdown of Daam1 in *Xenopus* disrupts nephron morphology without apparent effect on the

106   expression of genes related to early differentiation events (Miller et al., 2011). Differentiation

107   signals driving development of the nephric mesoderm in *Xenopus* largely function before the

108   onset of tubular morphogenesis (Vize et al., 2003). To further probe the mechanism by which

109   Daam1 regulates the shaping of nephrons, we analyzed the subcellular localization of

110   fluorescently tagged Daam1 at the beginning of tubular morphogenesis (around NF stage 30).

4

111 Through kidney-targeted microinjections that were targeted to early embryonic cells fated to

112 contributed to kidney (presumptive nephron progenitors) (DeLay et al., 2016; Moody and Kline,

113 1990), we expressed 1ng of fluorescently tagged Daam1 mRNA in the presumptive nephron

114 progenitors and analyzed its localization in fixed and live tissue.

115

116 For analyses of fixed tissue, embryos were subjected to whole-mount staining. The samples

117 were stained with an antibody against GFP to visualize Daam1, and an antibody against Lhx1 to

118 label nephron progenitors (DeLay et al., 2018; Venegas-FERRÍN et al., 2010). An additional

119 staining with Phalloidin allowed us to visualize the F-actin cytoskeleton, or alternatively, another

120 antibody was used to define the localization of E-cadherin **(Figure 1)**. Consistent with its

121 previously reported subcellular localization in other cell types (Corkins et al., 2019; Higashi et

122 al., 2019; Jaiswal et al., 2013; Kawabata Galbraith et al., 2018; Kida et al., 2007; Nishimura et

123 al., 2012, 2016), Daam1 co-localizes with patches of F-actin, showing a more diffuse staining

124 pattern in the cytoplasm and a strong localization to cell junctions **(Figure 1A)**. Furthermore,

125 co-immunostaining for GFP and E-cadherin demonstrated that E-cadherin is expressed within

126 the nephric primordium and it co-localizes with Daam1 at the cell-cell junctions **(Figure 1B)**.

127

128 During the early stages of development, the opaqueness of the *Xenopus* epithelium hinders

129 imaging of fluorescent protein expression in internal tissues, including the pronephric

130 primordium. In fixed tissues, this is overcome by using clearing agents such as BA:BB (1:2

131 mixture of benzyl alcohol and benzyl benzoate, aka Murray's clear). However, this process

132 requires dehydration of samples in methanol or ethanol prior to clearing, which is incompatible

133 with the use of fluorescent phalloidins (Becker and Gard, 2006). To overcome this obstacle, we

134 briefly washed embryos (< 20 sec) in isopropanol prior to clearing with BA:BA (Nworu et al.,

135 2014; Strickland et al., 2004). This allowed us to visualize Daam1 in conjunction with F-actin in

136 intact pronephric primordium **(Figure 1A)**.

137

138   To overcome an analogous challenge in live embryos, we developed a novel way of imaging the

139   nephric primordium *in vivo* **(Figure 2A)**. Previous studies have used the "windowed" embryo

140   approach consisting of microsurgical removal of the surface ectoderm to expose and image

141   underlying tissue (Kim and Davidson, 2013). Adopting this approach, we created "kidney-

142   windowed" embryos by removing the surface epithelium and exposing the underlying nephric

143   primordium for high-resolution *in vivo* imaging. *In vivo* time-lapse imaging of "kidney-windowed"

144   embryos showed GFP-Daam1 localizing to the cell-cell junctions. However, we observed that

145   GFP-Daam1 also localized to cytoplasmic vesicles and cellular protrusions **(Figure 2B, Video**

146   **S1)**. These observations are in line with previous reports on Daam1's localization and likely

147   hindered in imaging of fixed tissue due to unfavorable fixation conditions for observations of

148   cytoplasmic vesicles and cellular protrusions (Corkins et al., 2019; Jaiswal et al., 2013;

149   Kawabata Galbraith et al., 2018; Kida et al., 2007; Nishimura et al., 2012, 2016). Moreover, to

150   better understand the dynamics of Daam1 in the context of cell junctions, we imaged *de novo*

151   formation of cell-cell junctions in dissociated GFP-Daam1 expressing cells derived from the

152   nephric primordia **(Figure 2A).** *In vivo* time-lapse analyses of these cells showed that Daam1

153   localizes to filopodia-like protrusions and subsequently, to newly formed junctions **(Figure 2B,**

154   **Video S2)**.

155

156   Finally, we assessed the localization of Daam1 in the mature epithelium of fully developed

157   nephrons **(Figure S1).** Interestingly and importantly, junctional localization of Daam1 was not

158   detected in the mature epithelium. Taken together, these data suggested the potential role for

159   Daam1 in regulating the intercellular adhesion of renal progenitors specifically at the onset of

160   tubulogenesis and CE.

161

162 **Daam1 controls the organization and assembly of junctional F-actin within the nephric**

163 **primordium**

164 The observation that Daam1 co-localizes with junctional F-actin in developing *Xenopus*

165 nephron, led us to ask whether Daam1 regulates F-actin. To address this, we depleted Daam1

166 in nephron progenitors by utilizing Morpholino (MO) oligos in kidney-targeted microinjections

167 (DeLay et al., 2016; Moody and Kline, 1990). A proven Daam1 MO or an established Control

168 (standard) MO (Habas et al., 2001; Liu et al., 2008; Miller et al., 2011) was co-injected with a

169 membrane tagged GFP (mGFP) mRNA, that served as a linage tracer. MO-injected embryos

170 were fixed at the onset of tubular morphogenesis (around NF stage 30) and subjected to whole-

171 mount fluorescent staining and high-resolution confocal imaging. To verify the success of our

172 injections and knockdowns, we also carried out Western blot analyses of total protein lysates

173 prepared from stage 30 MO-injected embryos **(Figure 3B)**. Phalloidin staining revealed that

174 upon Daam1 depletion, the F-actin in renal progenitors becomes disorganized and significantly

175 reduced at cell-cell junctions **(Figure 3A and 3C, Videos S3 and S4).** These results suggest

176 that Daam1 contributes to the organization of the F-actin cytoskeleton and actin filaments at

177 cell-cell junctions during nephron development.

178

179 We also observed alterations in spatial positioning and the overall organization of nephron

180 progenitors upon depletion of Daam1. Nephric primordia in Daam1-morphants consist of fewer

181 progenitor cells **(Figure 3D)** that are spaced farther part from one another **(Figure 3E)**

182 compared to control animals. In addition to changes in the number and position of nephron

183 progenitors, we also noted changes in cell morphology. Nephric progenitors with diminished

184 Daam1 activity display an increase in cell area **(Figure 3F)** and circularity **(Figure 3G)**.

185

186 Since polymerization of F-actin filaments is a highly dynamic process, and to better understand

187 possible mechanisms underlying the observed morphological perturbations, we next assessed

188   the dynamic behavior of F-actin *in vivo* using fluorescence recovery after photobleaching

189   (FRAP) assays. We labeled F-actin in developing nephrons by co-injecting mCherry tagged

190   Utrophin (mCherry-UtrCH) mRNA (Burkel et al., 2007) along with control or Daam1 morpholino.

191   To probe F-actin dynamics in the context of the intact animal, we utilized the "kidney-windowed"

192   approach in NF stage 30 embryos. Overall, FRAP experiments suggest slower turnover of

193   junctional F-actin in Daam1-depleted nephrons in comparison with controls **(Figure 4)**. In

194   control nephrons, 100% of bleached cell junctions successfully recover fluorescence signal.

195   Whereas, in Daam1-depleted nephrons, only 59% of bleached junctions recovered **(Figure 4A)**.

196   Cell-cell junctions are comprised of dynamically mosaic E-cadherin clusters coupled to different

197   actin dynamics (Cavey et al., 2008; Indra et al., 2018). Therefore, the differences observed in

198   the dynamics of F-actin in Daam1 knockdown contexts potentially indicate the existence of two

199   actin pools differentially regulated by Daam1. However, it also possible that the observed

200   differences stem from the cell heterogeneity (e.g. in respect to Daam1 expression levels or cell-

201   type representation) within the nephric primordium. As we were unable to quantitatively assess

202   F-actin dynamics in junctions that fail to recover, we only used junctions with detectable

203   recovery signal to determine the mean half-time to recovery **(Figure 4D)** and the mean mobile

204   fraction **(Figure 4E)** values. For each junction values were taken from individually fitted curves.

205   These data indicate that the mean recovery half-time for junctional F-actin in Daam1 KD

206   nephrons is significantly slower (5.57 sec ± 0.99 s.e.m.) in comparison with control nephrons

207   (3.70 sec ± 0.35 s.e.m.) **(Figure 4D)**. In contrast, the mean mobile fractions are relatively similar

208   (56.0% ± 4.2 s.e.m for control and 54.3 % ± 4.5 s.e.m for Daam1 KD) **(Figure 4E)**. From these

209   data, we conclude that Daam1 is driving the rate of F-actin turnover to promote polymerization

210   of junctional actin during nephron development. Moreover, these data also suggest that the

211   decrease in F-actin fluorescence levels observed upon Daam1 depletion is likely a

212   consequence of impaired actin assembly.

213

214 **Daam1 promotes localization of E-cadherin at cell-cell contacts**

215 The interplay between E-cadherin and the actin cytoskeleton promotes intercellular adhesion

216 and assembly of cellular junctions. Therefore, we asked whether the changes observed in

217 junctional F-actin dynamics upon the knockdown of Daam1 alters the intercellular adhesion

218 between nephron progenitors. To examine if Daam1 regulates intercellular adhesion, we

219 analyzed the effect of Daam1 depletion on E-cadherin localization in developing nephron

220 **(Figure 5)**. Daam1 morphants displayed reduced levels of E-cadherin at the interfaces between

221 neighboring cells during these early stages of pronephric morphogenesis **(Figure 5A)**. This

222 difference was quantified and likewise made evident by measuring the fluorescence intensity

223 profiles of E-cadherin along the length of individual junctions **(Figure 5B)**. Of note and in

224 contrast, there was no difference in the overall E-cadherin protein levels between Daam1

225 knockdown and control embryos as determined by Western blotting **(Figure 5C).** These findings

226 suggest that Daam1 is likely more important for localization of E-cadherin at cell-cell contacts as

227 opposed to regulating the overall expression levels of E-cadherin.

228

229 Interestingly, Daam1 depleted cells remain capable of forming nephrons. Studies carried out in

230 MDCK cells using the pan-formin inhibitor SMIFH2 suggest that formins are required for early,

231 but not later stages of cell-cell adhesion (Collins et al., 2017). Moreover, Daam1 depleted

232 mammary epithelial cells form a monolayer characterized by irregular tilting of lateral cell

233 membranes and distorted cell morphology (Nishimura et al., 2016). To further understand the

234 function of Daam1 in nephron assembly, we analyzed the epithelium of mature nephrons in NF

235 stages 39-40 embryos **(Figure S2)**. Indeed, we did not observe any apparent changes in the

236 local concentration of junctional E-cadherin in mature nephrons of Daam1 knockdown and

237 control embryos **(Figure S2A).** However, Daam1 knockdown nephrons displayed defects in the

238 size of the tubular lumen. The diameter of tubular lumens was more variable in Daam1 deficient

239 nephrons compared to the controls**.** Similar to observations in mammary epithelial cells

9

240 (Nishimura et al., 2016), tubular cells in Daam1 depleted nephrons are less uniform in shape

241 and characterized by an irregular tilting of lateral cell membranes **(Figure S2A; Videos S5 and**

242 **S6).** We further found that when visualized by transmission electron microscopy (TEM), Daam1

243 depleted cells appear less columnar, characterized by indistinct and wavy cell borders **(Figure**

244 **S2B)**. Our results suggest that Daam1 regulates the adhesion between nephron progenitor cells

245 and subsequently, the morphology of the mature nephric epithelium.

246

247 **E-cadherin localization is mediated by the Daam1 FH2 domain**

248 Daam1 is known to act upstream of small Rho-GTPases, which regulate the actin cytoskeleton

249 (Habas et al., 2001; Liu et al., 2008); therefore, we next tested the importance of the actin

250 polymerization activity of Daam1 in intercellular adhesion. Formins are defined by a conserved

251 Formin Homology 2 (FH2) domain. The Daam1 forms a dimer via its FH2 domain, responsible

252 for nucleation and elongation of actin filaments (Lu et al., 2007; Yamashita et al., 2007). The

253 mutation isoleucine-to-alanine (Ile698Ala) in the Daam1 FH2 domain abolishes the actin

254 polymerization activity of Daam1 *in vitro* (Lu et al., 2007) and *in vivo* (Liu et al., 2008; Nishimura

255 et al., 2016). In kidney targeted-injections, we expressed either full-length GFP-Daam1 or GFP-

256 Daam1 FH2 mutant (Ile698Ala) mRNA and analyzed the effect on E-cadherin localization in the

257 nephric progenitors **(Figure 6).** Nephric progenitors expressing GFP-Daam1 FH2 mutant mRNA

258 showed reduced levels of E-cadherin at the interfaces between neighboring cells in comparison

259 to nephric progenitors expressing GFP-Daam1 **(Figure 6A-B)**. However, the E-cadherin

260 phenotype appeared to be less prominent than in Daam1 knockdown. Functional studies

261 showed that while an isoleucine-to-alanine mutation within FH2 domain abolishes Daam1's

262 ability to polymerize actin, it does not prevent its activation of Rho (Liu et al., 2008). This could

263 be one possible explanation as to why E-cadherin localization is more affected in Daam1

264 knockdown nephric progenitors. Furthermore, we assessed Daam1 protein levels in injected

265 embryos to determine if the observed differences in E-cadherin localization were potentially due

10

266 to underlying disparities in translation efficiency or protein stability of GFP-Daam1 and GFP-

267 Daam1 FH2 mutant **(Figure 6C)**. We found that Daam1 protein was present at equivalent levels

268 in the two samples, making these possibilities unlikely. Ultimately, the GFP-Daam1 FH2 mutant

269 expressing progenitors mature into nephrons characteristic of Daam1 knockdown **(Figure S3)**.

270 These results establish that the Daam1 FH2 domain is necessary for the localization of E-

271 cadherin to cell-cell contacts in nephron progenitors.

272

273 **Daam1 mediates cohesion of MDCK cells**

274 Nephron morphogenesis is achieved through the process called convergent extension (CE)

275 (Lienkamp et al., 2012). The CE is a type of collective cell movement characterized by a series

276 of coordinated and directed cell rearrangements (Huebner and Wallingford, 2018; Tada and

277 Heisenberg, 2012). In recent years E-cadherin has emerged as a key mediator for coordinating

278 cohesion and directional persistence of collective cell movements in both epithelial and

279 mesenchymal clusters (Cai et al., 2014; Campbell and Casanova, 2015; Cohen et al., 2016).

280 Our results demonstrate that Daam1 is necessary for the organization of nephrogenic

281 primordium **(Figure 3)** and a proper localization of E-cadherin **(Figures 5 and 6)**; therefore, we

282 wanted to determine if Daam1 is necessary for the coordination of direction between renal cells.

283 Because the opaqueness of *Xenopus* nephron progenitors prevents *in vivo* tracking of their

284 movements in 3D, we utilized Madin-Darby Canine Kidney (MDCK) cells. We generated MDCK

285 cells constitutively expressing an shRNA against Daam1 and analyzed whether the E-cadherin

286 localization is affected in these cells **(Figures 7A and S4)**. The efficiency of shDaam1

287 knockdown was confirmed by Western blot **(Figure 7B)**. Similar to what we saw in *Xenopus*

288 nephrons, we observed impaired localization of E-cadherin in nascent **(Figure 7A)**, but not

289 mature adhesions **(Figure S4)** upon knockdown of Daam1. We next examined the migratory

290 behavior of Daam1 knockdown cells in a time-lapse imaging of the wound-healing assay

291 **(Figure 7C-F; Video S7)**. We found Daam1 knockdown cells exhibit a delay in a wound closure

11

292   compared to control cells **(Figure 7C; Video S7)**. Additionally, we also observed random

293   detachment of Daam1-deficient cells from the migrating epithelial sheets **(Video S7).** To better

294   understand the behavior of these cells, we tracked their movement within the migrating sheets

295   over time. **(Figure S7)**. From these tracks, we obtained the relative distances over which cells

296   traveled and used those distances to assess cell velocities **(Figure 7C)**. These analyses show

297   that the speed at which Daam1 knockdown cells move is higher than that of the control cells,

298   demonstrating that delayed wound closure in Daam1 knockdown cells is not caused by their

299   slow movement. However, mapping the trajectory paths for Control **(Figure 7E)** and shDaam1

300   **(Figure 7D)** cells revealed that the movement of Daam1-deficient cells is less directed

301   compared to control. These data demonstrate that Daam1 is necessary for communication of

302   direction between the cells. Taken together, these results indicate that Daam1 contributes to

303   cohesion by regulating connectiveness of cells through E-cadherin.

304

305   **DISCUSSION**

306   Using *Xenopus* embryonic kidney and MDCK cells as model systems, we show that Daam1

307   mediates E-cadherin dependent intercellular adhesion and organization of nephrogenic

308   primordia by regulating polymerization of junctional actin filaments. Ultimately, this affects the

309   morphology of mature nephric epithelium. These findings have a number of important

310   implications for the regulation of intercellular adhesion and epithelial tubulogenesis.

311

312   First, we show that both Daam1 and E-cadherin localize to cell-cell contacts during nephron

313   development and that Daam1 is required for promoting E-cadherin localization at sites of cell-

314   cell contact. In contrast to what we observed during these early stages of nephron development

315   following the depletion of Daam1, in mature nephrons, we were unable to detect junctional

316   Daam1, and we likewise did not observe the effect on localization of E-cadherin. These data

317   suggest that Daam1 is necessary for efficient localization of E-cadherin at cell junctions in

318   nephron progenitor cells during early stages of nephron morphogenesis.

319

320   This conclusion builds upon certain assumptions. For example, it is possible that the

321   overexpression of GFP-Daam1 has an impact on our localization analyses, or that cells

322   depleted of Daam1 in mature nephrons are starting to recover due to a decrease in available

323   morpholino pools with time. However, multiple lines of evidence suggest that both of these

324   scenarios are highly unlikely. In the first case, prior studies indicate that the overexpression of

325   full length Daam1 has little to no affect the actin cytoskeleton or other cellular processes (Liu et

326   al., 2008). Additionally, several studies demonstrate that the distribution of the GFP-Daam1

327   recapitulates its endogenous localization as discerned via immunostaining (Jaiswal et al., 2013;

328   Li et al., 2011; Nishimura et al., 2012, 2016). In the second case, consistent with our

329   observations in *Xenopus* nephrons, sub-confluent cultures of MDCK cells stably expressing

330   shDaam1 show transient repression of E-cadherin localization to cell-cell contacts that appears

331   to be lost as the cells become confluent.

332

333   Indeed, our data support recent findings suggesting that actin nucleating proteins and Rho

334   GTPases are required for early stages of E-cadherin mediated cell-cell adhesion in MDCK

335   epithelial cells and not the maintenance of mature junctions (Collins et al., 2017). They also

336   imply that morphological defects that we see in mature nephrons are consequences of earlier

337   events. It is interesting to note that in similar fashion the silencing of E-cadherin expression in

338   MDCK cells disrupts formation of cell-cell junctions whereas its signaling seems to be largely

339   dispensable in already established epithelium as long as the cells are not mechanically stressed

340   (Capaldo and Macara, 2007).

341

13

342   Second, we show that Daam1 localizes to actin protrusions and newly formed cell-cell contacts

343   in developing nephron, suggesting that Daam1 via E-cadherin coordinates the assembly of cell-

344   cell junctions during CE. Actin polymerization at the cell's membrane mediates polarized

345   movement and intercalation of cells during CE through engagement of cadherins (Huebner and

346   Wallingford, 2018; Huebner et al., 2020). Here, we show that Daam1 activity functions to ensure

347   proper organization and size of nephrogenic primordium at the time of CE as well as polarized

348   movement of renal epithelial sheets. Our data support previous studies implicating Daam1 in CE

349   and polarized cell movements (Ang et al., 2010; Kida et al., 2007; Liu et al., 2008). Furthermore,

350   we show that Daam1 mediates polarized movement and cohesion of MDCK cells without

351   slowing down the motility of individual cells. Taken together these data suggest that Daam1

352   promotes collective cell movements by controlling actin's polymerization at cell-cell contacts and

353   strengthening of E-cadherin-based adhesion.

354

355   Finally, Wnt9b and Wnt11 regulate tubular nephron morphogenesis, and disruptions in the cell

356   behaviors traditionally regulated by the PCP pathway define their loss-of-function phenotypes

357   (Karner et al., 2009; O'Brien et al., 2018). We show that inhibiting signaling activity of Daam1 in

358   the prospective nephron results in a set of phenotypic characteristic comparable to those

359   reported for Wnt11 and Wnt9b. Moreover, earlier studies have demonstrated that Daam1 can

360   rescue Wnt11- induced CE gastrulation defects (Liu et al., 2008). These data collectively point

361   to Daam1 as a potential downstream effector of Wnt11 and Wnt9b signaling in the control of

362   nephric tubulogenesis. Interestingly, *wnt9b* and *wnt9a* are also induced in the injured nephrons

363   and a mutation in *fzd9b* is associated with reduced regenerative capacity of nephric tubules

364   (Kamei et al., 2019). These findings also suggest a potential role for Daam1 in repair and

365   regeneration of nephric tubules. This hypothesis is further supported by increasing research

366   evidence that the actin-based protrusions are important for the repair of cell-cell junctions (Li et

367   al., 2020) and studies showing that Daam1 promotes assembly of actin-based protrusions

368   (Jaiswal et al., 2013; Nishimura et al., 2016).

369

370   Cadherin localization is a complex process, and current studies propose at least three different

371   ways of achieving efficient localization of E-cadherin: (1) clustering enforced by cortical F-actin,

372   (2) clustering regulated by exposure of neighboring cells through their actin-based protrusions

373   and (3) clustering promoted by condensation of F-actin networks via myosin (Yap et al., 2015).

374   However, further research into timely regulation of E-cadherin is required to characterize the

375   precise molecular details and specify relationships between different modes of E-cadherin

376   clustering. Ultimately, investigations into how regulation of junctional E-cadherin by Daam1 fits

377   in with different modes of E-clustering will also be important to examine in the future.

378

379   **ACKNOWLEGMENTS**

398

399 **AUTHOR CONTRIBUTIONS**

400 V.K.S. conceived of the project, preformed experiments, analyzed data and wrote the original

401 draft of the manuscript. M.E.C. cloned pCS2-mCherry-Daam1 and pCS2-mCherry-Daam1

402 (Ile698Ala) constructs and contributed to data validation. V.K.S., M.E.C., A.B.G. and R.K.M.

403 preformed experiments to generate MDCK shDaam1 cells. V.K.S. and A.P. imaged the wound

404 healing assays, FRAP experiments and analyzed FRAP data. V.K.S. and M.K. conducted TEM

405 imaging analyses. A.B.G. and R.K.M. oversaw the experiments and supervised the project. All

406 authors were involved in critical evaluation and editing of the manuscript.

407

408 **DECLARATION OF INTERESTS**

409 The authors declare no competing interests.

410
411
412 **FIGURE TITLES AND LEGENDS**

413
414 **Figure 1. Daam1 co-localizes with junctional F-actin and E-cadherin during early nephron
415 development**

416
417 Confocal maximum image projections of whole-mount immunostaining of *Xenopus* nephric

418 primordium labeled by Lhx1(magenta) and GFP to visualize Daam1 (green) in conjunction with,
419
420 (A) Phalloidin staining to visualize F-actin (red) or

421
422 (B) E-cadherin (cyan);

423
424 a'-a''' and b'-b''' represent close-up images of white boxes.

425
426

16

427 **Figure 2. Daam1 localizes to newly formed cell-cell contacts**

428 (A) Schematic illustration showing steps involved in preparation of "windowed kidney" embryos

429 and primary cultures expressing GFP-Daam1. Please note that for clarity of illustration the 8-cell

430 GFP-Daam1 injected *Xenopus* blastomere is fate-mapped strictly to the nephric primordium and

431 that blastomere also contributes to epidermis, ventral and dorsal somites, hidgut, proctodeum

432 and trunk neural crest cells (DeLay et al., 2016; Moody and Kline, 1990).

433 (B) Time-lapse imaging montage of the nephric primordium expressing GFP-Daam1 in

434 "windowed kidney" embryos. Elapsed time is indicated at the top in seconds; see **Video S1**.

435 (C) Time-lapse imaging montage shows cells isolated from a developing nephron expressing

436 GFP-Daam1 mRNA adhering with each other. Elapsed time is indicated at the top in seconds.

437 The border arising between two cells is delineated by the red dotted line; see **Video S2**.

438
439 **Figure 3. Effects of Daam1 depletion on the nephrogenic primordium**
440
441 (A) Maximum projection confocal images of F-actin expression (red) in nephric primordium

442 (magenta) in Control and Daam1 knockdown embryos. a-a'' and b'-b'' represent close-up

443 images of the corresponding regions in white boxes; see **Videos S3 and S4**.

444 (B) Western blot showing Daam1 and GAPDH (control) protein levels for uninjected wild type

445 (WT) and Control (Standard morpholino) and Daam1 KD (Daam1 morpholino) injected embryos.

446 (C) The graph showing the relative fluorescence intensity levels of junctional F-actin in the

447 nephric primordia of Control and Daam1 KD embryos. $N_{Control}$=40 junctions on 2 embryos and

448 $N_{Daam1\ KD}$=40 junctions on 2 embryos. ****$P < 0.0001$ analyzed by unpaired t-test.

449 (D-G) Morphometric analyses of Control and Daam1-depleted nephric primordia. The thick bars

450 represent the mean, ****$P < 0.0001$ analyzed by unpaired t-test, (E-G) $N_{Control}$=40 junctions on 2

451 embryos and $N_{Daam1\ KD}$=40 junctions on 2 embryos. Graphs showing comparison between

452 Control and Daam1-depleted nephric primordia of,

453 (D) the average number of Lhx1-positive nephron progenitors where $N_{Control}$=5 embryos and

454 $N_{Daam1KD}$=5 embryos,

455 (E) the relative distance between nearest neighbors of Lhx1-positive nuclei,

17

456   (F) the relative cell area and

457   (G) the relative circularity, where 1 represents the perfect circle.

458
459   **Figure 4. Daam1 regulates assembly of junctional F-actin in developing nephron**
460
461   F-actin dynamics at cell-cell junctions of Control and Daam1-depleted developing nephrons

462   expressing mCherry-Utrophin were assessed using FRAP.

463   (A) Percentage of junctions showing recovery of fluorescence after bleaching in Control (black,

464   N_{total}=27 junctions, 1-5 junctions/embryo) and Daam1 KD (purple and orange, N_{total}=27 junctions,

465   1-5 junctions/embryo) nephrons.

466   (B) Typical time-lapse images of Control and Daam1-depleted cell junctions before and after

467   photobleaching. In each image, the bleached region is highlighted with a circle (black - Control

468   junction showing recovery, purple - Daam1 KD junction showing recovery and orange - Daam1

469   KD junction showing no-recovery of fluorescence after photobleaching).

470   (C) Graph shows average recovery curves obtained from individual best-fit plots for Control

471   (black), Daam1 KD junctions with (purple) and without (orange) recovery of fluorescence after

472   photobleaching.

473   (D-E) Bar graphs comparing Control and Daam1 KD profiles calculated from individual best-fit

474   curves for Control (black) and Daam1 KD junctions with recovery of fluorescence after

475   photobleaching (purple). Data represent the mean ± S.E. from three independent experiments.

476   P-values were analyzed by unpaired t-test.

477   (D) Bar graph of the relative half-times for F-actin.

478   (E) Bar graph of the relative mobile fraction for F-actin.

479
480   **Figure 5. Daam1 promotes localization of junctional E-cadherin**
481
482   (A) Maximum projection confocal images of E-cadherin expression (cyan) in nephric primordium

483   (magenta) in Control and Daam1 KD embryos a-a' and b-b' represent the close-up images of

484   corresponding regions in white boxes.

18

(B) Violin plots depicting the relative fluorescence intensity of junctional E-cadherin in the nephric primordia of Control (orange) and Daam1 KD (blue). $N_{Control}=88$ junctions on 4 embryos and $N_{Daam1\ KD}=84$ junctions on 4 embryos. Center-lines represents median; Limits show 1_{st} and 3_{rd} quartile. ****P<0.0001 analyzed by unpaired t-test.

(C) Western blot showing Daam1, E-cadherin and GAPDH (control) protein levels in uninjected wild type (WT) and Control (Standard morpholino) and Daam1 KD (Daam1 morpholino) injected embryos.

Figure 6. E-cadherin localization to cell-cell junctions is mediated by FH2 domain of Daam1

(A) Maximum projection confocal images showing E-cadherin staining (cyan) in nephric primordium (magenta) expressing GFP-Daam1 or GFP-Daam1 FH2 mutant mRNA. a-a' and b-b' represent close-up images of corresponding regions in white boxes.

(B) Violin plots depicting the relative fluorescence intensity of junctional E-cadherin in the nephric primordia expressing GFP-Daam1 (orange) and GFP-Daam1 FH2 mutant (blue) mRNA. $N_{Daam1}=60$ junctions on 3 embryos and $N_{Daam1FH2mutant}=55$ junctions on 3 embryos. Center-lines represents median; Limits show 1_{st} and 3_{rd} quartile. ***P<0.0002 analyzed by unpaired t-test.

(C) Western blot showing the exogenous and endogenous protein levels of Daam1 in uninjected wild type (WT) embryos, embryos injected with 1 ng of GFP-Daam1 mRNA and 1ng GFP-Daam1 FH2 mutant mRNA. The non-specific band confirms equal loading.

Figure 7. Daam1- depleted MDCK cells display compromised localization of E-cadherin at cell-cell contacts and impaired cohesion during collective movement

(A) E-cadherin (green), F-actin (red) and DAPI (blue) in subconfluent the MDCK Control and shDaam1 knockdown cells. E-cadherin localization in the nascent cell-cell contacts (marked by white brackets and shown enlarged in corresponding white boxes) is impaired in shDaam1-deficient cells.

(B) Western blot analysis of Daam1 and GAPDH protein levels in the MDCK Control and shDaam1 knockdown cells.

(C-F) Summary of the wound-healing experiments for the MDCK Control and Daam1 KD cells, **see Video S7**.

19

519   (C) Daam1 depletion impairs wound closure. The graph represents the percent of the wound

520   surface area over time for Control (purple) and Daam1 KD (orange) cells. Error bars indicate

521   S.E. of the mean on 4 assays.

522   (D-F) Manually tracking migration paths of single-cells during the wound closure demonstrates

523   that Daam1 organizes collective movement of the MDCK epithelial monolayers by modulating

524   the speed and directionality of individual cells. Depletion of Daam1 results in increased velocity

525   and random migration. $N_{Control}$=52 cells from 4 assays and $N_{Daam1\ KD}$=42 cells tracked from 4

526   assays. Cells were tracked in 15 minutes increments for 12 hours.

527   (D) Violin plots represent migration velocity calculated from tracking traveled distances of single

528   cells for Control and Daam1 KD cells. Center-lines represents median; Limits show 1_{st} and 3_{rd}

529   quartile. ***P<0.0001 analyzed by unpaired t-test.

530   (E) Wind-rose plot showing migration tracks of individual Control cells.

531   (F) Wind-rose plot showing migration tracks of Daam1 KD cells.

532
533   **MATERIALS AND METHODS**
534

535   ***Xenopus laevis***

536   *Xenopus laevis* adult male and female frogs were obtained from Nasco (LM00531MX and

537   LM00713M) (Fort Atkins, WI, USA) and maintained according to standard procedures. *Xenopus*

538   embryos were obtained by *in vitro* fertilization (Sive et al., 2000) and staged as previously

539   described by Nieuwkoop and Faber (NF) (Nieuwkoop and Faber, 1994). All work was carried

540   out in accordance with the University of Texas Health Science Center at Houston, Institutional

541   Animal Care and Use Committee (IACUC) protocol #AWC-19-0081.

542

543   **MDCK cell lines**

544   Madin-Darby Canine Kidney (MDCK) II cell lines were purchased from the American Type

545   Culture Collection (ATCC). MDCK cells were cultured at 37ºC with 5% CO_2 in Dulbecco's

546 Modified Eagle's Medium (DMEM) (Sigma, D6429) supplemented with 10% fetal bovine serum

547 (FBS) (Sigma, F0926) and 1% Antibiotic-antimycotic solution (Sigma, A5955).

548

549 **Embryo microinjections**

550 *Xenopus* embryos were microinjected at one-cell or into V2 blastomere at eight-cell stage,

551 targeting embryonic kidney (DeLay et al., 2016; Moody and Kline, 1990; Nieuwkoop and Faber,

552 1994). Embryos were injected with synthetic mRNAs alone or in combination with antisense

553 morpholino oligonucleotides (MOs). For mRNA injections, capped mRNA transcripts were

554 synthesized from DNA-plasmids using SP6 mMessage mMachine transcription kit

555 (ThermoFisher, AM1340M) and purified. pCS2-GFP-Daam1 and pCS2-GFP-Daam1 (Ile698Ala)

556 plasmids were a gift from Dr. Raymond Habas's and Dr. Bruce Goode's labs, respectively (Lu et

557 al., 2007). A mutation A2822G discovered in these plasmids was corrected by site directed

558 mutagenesis as previously reported (Corkins et al., 2019) prior to mRNA synthesis. pCS2-

559 membrane-tagged-RFP (mRFP)(Davidson et al., 2006), pCS2-membrane-tagged-EGFP

560 (mEGFP)(Shindo and Wallingford, 2014) and pCS2-mCherry-Utrophin (mCherry-UtrCH)(Burkel

561 et al., 2007) constructs were gifts from Dr. Raymond Keller's lab, Dr. John Wallingford's lab and

562 Dr. William Bement's lab, respectively. Formerly developed translation-blocking Daam1

563 (5′GCCGCAGGTCTGTCAGTTGCTTCTA 3′) (Corkins et al., 2018; Habas et al., 2001; Miller et

564 al., 2011) and standard control (5′CCTCTTACCTCAGTTACAATTTATA 3′) MOs were

565 purchased from GeneTools, LLC (Philomath, OR, USA). MOs were injected at 20ng per embryo

566 while the amount of injected mRNA per embryo were as follows: GFP-Daam1 [1ng], mCherry-

567 Daam1 [1ng], GFP-Daam1(I698A) [1ng], mCherry-Daam1(I698A) [1ng], mRFP [0.5ng], mGFP

568 [0.5ng] and mCherry-UtrCH [1ng].

569

570 **Generation of stable MDCK shDaam1 cell lines**

571   shDaam1 knockdown cell lines were generated by a retrovirus-based transduction method as

572   described (Corkins et al., 2019). Briefly, the pLKO.1 lentiviral shDaam1 constructs

573   (TTTCAGGAGATAGTATTGTGC, AAACAGGTCTTTAGCTTCTGC) were purchased from GE-

574   Dharmacon (Clone ID: TRCN0000122999, Clone ID: TRCN0000123000). HEK293T cells were

575   co-transfected with shDaam1 and virus packaging plasmids (psPAX2 and pMD2.G) using

576   Polyethylenimine (PEI). The viral titers were collected starting 24 hours post transfection over

577   the course of two days and purified using 0.22 μm Polyethersulfone (PES) syringe filters.

578   Infections were carried out in the presence of polybrene. MDCK II cells remained in infection

579   media for 24 hours, followed by puromycin selection with final concentration of 0.70 μg/ml.

580   Lastly, MDCK II shDaam1 knockdown stable cell lines were validated by Western blotting.

581

582   **Western blotting**

583   Western blotting was carried out using published protocols (Kim et al., 2002; Williams et al.,

584   2017). In short, *Xenopus* embryos were cultured to desired stage and collected. The whole-

585   embryo lysates were prepared by resuspending 10-20 embryos in a prechilled TX100-lysis

586   buffer (10 mM HEPES, 150 mM NaCl, 2 mM EDTA, 2 mM EGTA, 0.5% Triton X-100, pH 7.4)

587   and centrifuged at 18,407 RCF at 4°C for 5 minutes. The resulting protein lysates were

588   resuspended in an equal volume 2X Laemmli (BioRad,161-0737) + dithiothreitol (Fisher

589   BioReagents, BP17225) solution, and incubated at 95°C for 2 minutes. For making protein

590   lysates using MDCK cells, cells were washed with PBS and pelleted by centrifugation at 18,407

591   RCF at 4°C for 5 minutes. Cell pellets were resuspended in in a prechilled Triton-lysis buffer (50

592   mM Tris pH 7.4, 1% Triton X-100, 150 mM NaCl, 1 mM EDTA, 1 mM EGTA, 1 mM PMSF, 1 mM

593   Na$_3$VO$_4$, 10 mM sodium fluoride, 10 mM β-glycerophosphate, 1 mg/ml aprotinin, and 1 mg/ml

594   leupeptin). The cell lysates were incubated on ice for 20 minutes, followed by sonication and

595   centrifugation at 18,407 RCF for 10 minutes at 4°C. Bradford assay was used to determine the

22

596   total amount of protein in the lysates. The protein samples were run on an 8% SDS-PAGE gel

597   and transferred to nitrocellulose or polyvinylidene difluoride (PVDF) membranes. The blots were

598   blocked for at least 1.5 hours at the room temperature using the KPL Detector Block Kit (Sera

599   Care, 5920-0004, 71-83-00) and probed with primary antibodies overnight at 4°C. The next day,

600   after series of washes with Tris-buffered saline containing 0.1% Tween 20 (TBST), blots were

601   incubated with secondary antibodies for at least 1 hour at the room temperature. Protein

602   expression levels were detected with enhanced chemiluminesence (SuperSignal West Pico

603   PLUS Chemiluminescent Substrate, Thermo Fisher, 34580) using LiCor and BioRad ChemiDoc

604   XRS imagers. The following antibodies were used: rabbit anti-Daam1 (1:1000, Proteintech,

605   14876-1-AP), rabbit anti-Daam1 (1:1000, gift from Dr. Raymond Habas), rabbit anti-GAPDH

606   (1:1000, Santa Cruz, sc-25778), mouse anti-E-cadherin (1:1000, BD Transduction Laboratories,

607   610182), rabbit anti-GFP (1:250, ICL Lab, RGFP-45A), anti-rabbit IgG (H + L)-HRP (1:5000,

608   BioRad,1706516) and anti-mouse IgG (H + L)-HRP (1:5000, BioRad, 1706516).

609

610   **Immunostaining and staining**

611   *Xenopus* embryos were fixed in MEMFA (3.7% formaldehyde, 4 mM MOPS, 2 mM EGTA, and 1

612   mM $MgSO_4$, pH 7.4) for 1 hour at room temperature or overnight at 4°C. Embryos to be stained

613   with Phalloidin, were fixed using methanol-free formaldehyde (Thermo Scientific, 28908).

614   Immunostaining was carried out according to previously published methods (Hemmati-Brivanlou

615   and Melton, 1994; Krneta-Stankic et al., 2010). In short, fixed-embryos were washed 3 times for

616   15 minutes at room temperature with phosphate buffered saline (PBS) containing 0.1% Triton X-

617   100 and 0.2% bovine serum albumin (BSA) and blocked using 10% goat serum diluted in PBST

618   for 1 hour at room temperature. Embryos were incubated with the primary antibodies overnight

619   at 4°C. The next day, embryos were washed 5 times for 1 hour with PBS-T at room temperature

620   and then incubated with the secondary antibodies overnight at 4°C. The following day, embryos

23

621   were washed 3 times for 1hr at room temperature and dehydrated in methanol prior to clearing.

622   To preserve Phalloidin-labeling, isopropanol was used to dehydrate Phalloidin-stained embryos

623   (Nworu et al., 2014). Embryos were cleared using BABB (1-part benzyl alcohol: 2-parts benzyl

624   benzoate) clearing solution and imaged. MDCK cells were fixed in 4% paraformaldehyde (PFA)

625   for 10 minutes at room temperature. Cultures were washed 3 times with PBS and incubated

626   with 50mM ammonium chloride for 10 minutes at room temperature to neutralize the PFA. Next,

627   samples were washed 3 times with PBS and blocked using 10% goat serum/ PBST for 1 hour

628   and incubated with primary antibodies overnight at 4°C. The following day, MDCK cells were

629   washed 3 times with PBS and incubated with secondary antibodies for 1 hour at room

630   temperature. Lastly, stained samples were washed again 3 times with PBS prior to mounting in

631   Fluoromount-G medium (Southern Biotech, 0100-01) for imaging. The following primary

632   antibodies were used: chicken anti-GFP (1:250, Abcam, ab13970), rabbit anti-RFP (1:250, MBL

633   International, PM005), rabbit anti-GFP (1:250, ICL Lab, RGFP-45A), rabbit anti-Lhx1 (1:250, gift

634   from Dr. Masanori Taira) and mouse anti-E-cadherin (1:100, BD Transduction Laboratories,

635   610182). For detection of primary antibodies the following secondary antibodies were used:

636   anti-rabbit IgG Alexa 488 (1:500, Invitrogen, A-11008), anti-rabbit IgG Alexa 555 (1:500,

637   Invitrogen, A-21428), anti-rabbit IgG Alexa 647 (1:500, Invitrogen, A-21244), anti-mouse IgG

638   Alexa 488 (1:500, Invitrogen, A-11001), anti-mouse IgG Alexa 555 (1:500, Invitrogen, A-21422),

639   anti-mouse IgG Alexa 647 (1:500, Invitrogen, A-21235), anti-mouse IgG Alexa 488 (1:500,

640   Jackson ImmunoResearch, 715-545-150) and anti-chicken IgY Alexa 488 (1:500, Invitrogen, A-

641   11039). Fluorescent probes used for staining were as follows: FITC-conjugated lectin from

642   *Erythrina cristagalli* (1:500, Vector labs, FL-1141), Phalloidin-Alexa 568 (embryos- 1:40 and

643   cells-1:200, Invitrogen, A12380), and diamidino-2-phenylindole (DAPI) (1:500, Thermo

644   Scientific, 62247).

645

646   **Transmission electron microscopy (TEM)**

647 *Xenopus* embryos were fixed in 2%formaldehyde+0.5% glutaraldehyde (Ted Pella Inc., 18505

648 and 18426). Fixed embryos were washed with 0.1 M sodium cacodylate buffer and treated with

649 0.1% Millipore-filtered cacodylate buffered tannic acid. Embryos were post-fixed using 1%

650 buffered osmium, followed by staining using 1% Millipore-filtered uranyl acetate. Stained

651 embryos were dehydrated by washing in increasing concentrations of ethanol, permeated, and

652 embedded in LX-112 medium. After embedding, embryos were placed in a 60°C oven for

653 approximately 3 days to polymerize. Polymerized samples were sectioned using Leica Ultracut

654 microtome (Leica, Deerfield, IL). Collected ultrathin sections were stained with uranyl acetate

655 and lead citrate in a Leica EM Stainer and subjected to imaging.

656

657 **Isolation and live imaging of *Xenopus* kidney cells**

658 Embryos were microinjected with 1ng GFP-Daam1 mRNA into the V2 blastomere, targeting

659 kidney. Around embryonic NF stage 30, GFP-positive nephrons were surgically dissected under

660 a fluorescent stereomicroscope using a pair of sharpened forceps (Fisher, NC9404145).

661 Microsurgical dissections were performed in plastic petri dishes coated with 2% agar containing

662 Danilchik's for Amy (DFA) solution (53 mM NaCl, 5 mM Na_2CO_3, 4.5 mM Potassium Gluconate,

663 32 mM Sodium Gluconate, 1 mM $CaCl_2$, 1 mM $MgSO_4$, buffered to pH 8.3 with 1 M bicine)

664 supplemented with 1 g/l of and Antibiotic antimycotic solution (1:100, Sigma, A5955). To

665 dissociate into single cells, the isolated nephrons were transferred to fibronectin coated (1μg/ml,

666 Roche, 10-838-039-001) glass-bottom imaging chambers (Thermo, A7816) prefilled with

667 Calcium Magnesium Free Media (CMFM) (88 mM NaCl, 1 mM KCl, 2.4 mM $NaHCO_3$, 7.5 mM

668 Tris pH 7.6). After ~30 minutes at the room temperature, as much as possible of the CMFM

669 media was aspirated from top of the chamber without disturbing the cells. Fresh DFA media was

670 added and again removed by careful aspiration. In order to ensure complete removal of the

671   CMFM media, this process was repeated at least 5 times. The cells were left undisturbed at the

672   room temperature for 15-30 minutes prior to imaging.

673

674   **Wound-healing assay**

675   MDCK cells were seeded in 6-well culture plates at a density of 100,000 cells/well and allowed

676   to reach confluency. Prior to inducing a "wound" or scratch or in a confluent cell monolayer, the

677   cells were treated with Mitomycin C (10 μg/ml) for 3 hours at 37$°$C to prevent future proliferation.

678   A linear scratch was made by gliding the 200 μl sterile tip across the bottom of each well. After

679   making a scratch, cells were washed with 1X PBS and refed with 5 ml of 10%FBS/DEMEM

680   supplemented with 1%Antibiotic-antimycotic solution. Samples were placed in 37$°$C heated

681   imaging chamber with 5% CO2 and subjected to time-lapse imaging.

682

683   **Fluorescence Recovery after Photobleaching (FRAP)**

684   To visualize actin dynamics, embryos were injected into V2 blastomere at 8-cell stage with 1 ng

685   mCherry-UtrCH mRNA along with 20 ng of Daam1 or Standard (control) MO. Injected embryos

686   were cultured to around NF stage 30. Since the opaqueness of *Xenopus* epithelium prevents

687   direct *in vivo* imaging of developing nephron at this early embryonic stage, "windowed" embryos

688   were generated. To make windowed embryos, embryos were anesthetized in 0.04% (0.15%)

689   Ethyl 3-aminobenzoate methanesulfonate (Sigma, E10521) diluted in DFA. Next, the epithelium

690   covering developing nephron was surgically removed under fluorescence-dissecting

691   microscope, exposing developing nephron for *in vivo* imaging. Windowed embryos were

692   mounted under glass-cover slips and subjected to FRAP. FRAP assays were performed on an

693   inverted 3i spinning disk microscope integrated to a NIKON TiE with perfect focus and equipped

694   with Vector™ FRAP scanning module and a Hamamatsu Flash 4.0 camera. Images were

695   acquired with a NIKON Plan-Apo 60X water 1.2 NA objective. A small fragment at the midpoint

696 of a cell-cell junction was bleached with the 561nm laser line at 100% power. A series of twenty

697 pre-bleach images were captured and post-bleach recovery was recorded continuously until

698 fluorescent signal reached a steady state. Movies were analyzed using Slidebook 6.0 and curve

699 fitting was done with SigmaPlot and GraphPad Prism 8.0 software. For curve fitting, a single

700 exponential function ($f(t)=\alpha(1-e_{-kT})$), where $T_{1/2}$ (half-time of recovery) is ln 0.5/(-k), and α is the

701 mobile fraction was used. Raw recovery curves were corrected for background and photofading.

702 Lowest fluorescence signal and the time-point after bleaching were scaled to 0 and curves were

703 normalized to 1 based on the reference signal before bleaching. Per embryo, between 1 and 5

704 single junctions were photobleached. To avoid bleaching-induced variation in fluorescence,

705 junctions picked for photobleaching were spaced far apart. All FRAP experiments have been

706 carried out using multiple embryos and repeated at least three times.

707

708 **Image acquisition and processing**

709 Olympus SZX16 fluorescent stereomicroscope equipped with Olympus DP71 camera was used

710 for carrying out *Xenopus* microsurgical manipulations, embryo mounts and scoring of kidney

711 phenotypes in NF stage 40 embryos. Zeiss LSM800 microscope with Airyscan detector,

712 LeicaSP5 and NikonA1 were used for confocal imaging of fixed and live samples. Captured

713 images and time-lapse movies were exported as original files and processed using ImageJ (Fiji

714 plugin). Image panels were built using FigureJ plugin. Final figures were assembled in Adobe

715 Photoshop CC. TEM imaging was carried out in a JEM 1010 transmission electron microscope

716 (JEOL, USA, Inc., Peabody, MA) with the AMT Imaging System (Advanced Microscopy

717 Techniques Corp, Danvers, MA).

718

719 **Quantification and statistical analyses**

720 ImageJ (Fiji plugin) software was used for quantitative image analyses. For quantification of E-

721 cadherin and F-actin staining **(Figures 3, 5 and 6)** images were captured using the same

722   settings. The mean fluorescence intensity along the length of selected junction was measured.

723   To analyze tissue organization during nephron development **(Figure 3)** cells were manually

724   counted using the Cell Counter tool. The shortest distance between two neighboring nuclei was

725   measured using the straight-line selection tool. The area and circularity were measured using

726   the Analyze Particles tool. Wound area **(Figure 7)** was also measured using the Analyze

727   Particles tool. To obtain traveled distance, trajectories of randomly selected cells were traced

728   manually in each frame of the time-lapse using Plugin for Motion Tracking and Analysis

729   (MTrackJ) (The Biomedical Imaging Group of Erasmus University Medical Centre, Rotterdam,

730   The Netherlands). All experiments were repeated at least two times, with the exception of TEM

731   studies, which due to the prohibitive costs of the experiment represent single-trial analyses. The

732   exact sample size and statistical analysis for each experiment are presented in the

733   corresponding figure legend. Statistical analyses were carried out using GraphPad Prism 8.0

734   software.

735
736
737
738   **REFERENCES**
739

740   Adams, C.L., Chen, Y.T., Smith, S.J., and Nelson, W.J. (1998). Mechanisms of epithelial cell-
741   cell adhesion and cell compaction revealed by high-resolution tracking of E-cadherin-green
742   fluorescent protein. J. Cell Biol. *142*, 1105–1119.

743   Ang, S.F., Zhao, Z.S., Lim, L., and Manser, E. (2010). DAAM1 is a formin required for
744   centrosome re-orientation during cell migration. PLoS One *5*, e13064.

745   Becker, B.E., and Gard, D.L. (2006). Visualization of the Cytoskeleton in Xenopus Oocytes and
746   Eggs by Confocal Immunofluorescence Microscopy. In Methods Mol Biol., pp. 69–86.

747   Burkel, B.M., von Dassow, G., and Bement, W.M. (2007). Versatile fluorescent probes for actin
748   filaments based on the actin-binding domain of utrophin. Cell Motil. Cytoskeleton *64*, 822–832.

749   Cai, D., Chen, S.-C., Prasad, M., He, L., Wang, X., Choesmel-Cadamuro, V., Sawyer, J.K.,
750   Danuser, G., and Montell, D.J. (2014). Mechanical feedback through E-cadherin promotes
751   direction sensing during collective cell migration. Cell *157*, 1146–1159.

752   Campbell, K., and Casanova, J. (2015). A role for E-cadherin in ensuring cohesive migration of
753   a heterogeneous population of non-epithelial cells. Nat. Commun. *6*, 7998.

754   Campbell, K., and Casanova, J. (2016). A common framework for EMT and collective cell
755   migration. Dev. *143*, 4291–4300.

756   Capaldo, C.T., and Macara, I.G. (2007). Depletion of E-Cadherin Disrupts Establishment but

Not Maintenance of Cell Junctions in Madin-Darby Canine Kidney Epithelial Cells. Mol. Biol. Cell *18*, 189–200.

Castelli, M., Boca, M., Chiaravalli, M., Ramalingam, H., Rowe, I., Distefano, G., Carroll, T., and Boletta, A. (2013). Polycystin-1 binds Par3/aPKC and controls convergent extension during renal tubular morphogenesis. Nat. Commun. *4*, 1–10.

Cavey, M., Rauzi, M., Lenne, P.F., and Lecuit, T. (2008). A two-tiered mechanism for stabilization and immobilization of E-cadherin. Nature *453*, 751–756.

Cohen, D.J., Gloerich, M., and Nelson, W.J. (2016). Epithelial self-healing is recapitulated by a 3D biomimetic E-cadherin junction. Proc. Natl. Acad. Sci. U. S. A. *113*, 14698–14703.

Collins, C., Denisin, A.K., Pruitt, B.L., and Nelson, W.J. (2017). Changes in E-cadherin rigidity sensing regulate cell adhesion. Proc. Natl. Acad. Sci. U. S. A. *114*, E5835–E5844.

Combes, A.N., Davies, J.A., and Little, M.H. (2015). Cell-cell interactions driving kidney morphogenesis. Curr. Top. Dev. Biol. *112*, 467–508.

Corkins, M.E., Hanania, H.L., Krneta-Stankic, V., Delay, B.D., Pearl, E.J., Lee, M., Ji, H., Davidson, A.J., Horb, M.E., and Miller, R.K. (2018). Transgenic Xenopus laevis line for in vivo labeling of nephrons within the kidney. Genes (Basel). *9*, 197.

Corkins, M.E., Krneta-Stankic, V., Kloc, M., McCrea, P.D., Gladden, A.B., and Miller, R.K. (2019). Divergent roles of the Wnt/PCP Formin Daam1 in renal ciliogenesis. PLoS One *14*, e0221698.

Davidson, L.A., Marsden, M., Keller, R., and DeSimone, D.W. (2006). Integrin α5β1 and Fibronectin Regulate Polarized Cell Protrusions Required for Xenopus Convergence and Extension. Curr. Biol. *16*, 833–844.

DeLay, B.D., Krneta-Stankic, V., and Miller, R.K. (2016). Technique to Target Microinjection to the Developing Xenopus Kidney. J. Vis. Exp. *111*.

DeLay, B.D., Corkins, M.E., Hanania, H.L., Salanga, M., Deng, J.M., Sudou, N., Taira, M., Horb, M.E., and Miller, R.K. (2018). Tissue-Specific Gene Inactivation in Xenopus laevis: Knockout of lhx1 in the Kidney with CRISPR/Cas9. Genetics *208*, 673–686.

Friedl, P., and Mayor, R. (2017). Tuning Collective Cell Migration by Cell–Cell Junction Regulation. Cold Spring Harb. Perspect. Biol. 1–17.

Grikscheit, K., and Grosse, R. (2016). Formins at the Junction. Trends Biochem. Sci. *41*, 148–159.

Habas, R., Kato, Y., and He, X. (2001). Wnt/Frizzled activation of Rho regulates vertebrate gastrulation and requires a novel Formin homology protein Daam1. Cell *107*, 843–854.

Hemmati-Brivanlou, A., and Melton, D.A. (1994). Inhibition of activin receptor signaling promotes neuralization in Xenopus. Cell *77*, 273–281.

Higashi, T., Stephenson, R.E., and Miller, A.L. (2019). Comprehensive analysis of formin localization in Xenopus epithelial cells. Mol. Biol. Cell *30*, 82–95.

Huebner, R.J., and Wallingford, J.B. (2018). Coming to Consensus: A Unifying Model Emerges for Convergent Extension. Dev. Cell *46*, 389–396.

Huebner, R.J., Malmi-kakkada, A.N., Sarikaya, S., Weng, S., and Wallingford, J.B. (2020). Cadherin clustering controls heterogeneous , asymmetric junction dynamics during vertebrate axis elongation. BioRxiv 2020.02.11.944033.

Indra, I., Choi, J., Chen, C.S., Troyanovsky, R.B., Shapiro, L., Honig, B., and Troyanovsky, S.M. (2018). Spatial and temporal organization of cadherin in punctate adherens junctions. Proc.

801   Natl. Acad. Sci. U. S. A. *115*, E4406–E4415.

802   Jaiswal, R., Breitsprecher, D., Collins, A., Corrêa, I.R., Xu, M.Q., and Goode, B.L. (2013). The
803   formin daam1 and fascin directly collaborate to promote filopodia formation. Curr. Biol. *23*,
804   1373–1379.

805   Kamei, C.N., Gallegos, T.F., Liu, Y., Hukriede, N., and Drummond, I.A. (2019). Wnt signaling
806   mediates new nephron formation during zebrafish kidney regeneration. Dev. *146*.

807   Karner, C.M., Chirumamilla, R., Aoki, S., Igarashi, P., Wallingford, J.B., and Carroll, T.J. (2009).
808   Wnt9b signaling regulates planar cell polarity and kidney tubule morphogenesis. Nat. Genet. *41*,
809   793–799.

810   Kawabata Galbraith, K., Fujishima, K., Mizuno, H., Lee, S.J., Uemura, T., Sakimura, K.,
811   Mishina, M., Watanabe, N., and Kengaku, M. (2018). MTSS1 Regulation of Actin-Nucleating
812   Formin DAAM1 in Dendritic Filopodia Determines Final Dendritic Configuration of Purkinje Cells.
813   Cell Rep. *24*, 95-106.e9.

814   Kida, Y.S., Sato, T., Miyasaka, K.Y., Suto, A., and Ogura, T. (2007). Daam1 regulates the
815   endocytosis of EphB during the convergent extension of the zebrafish notochord. Proc. Natl.
816   Acad. Sci. U. S. A. *104*, 6708–6713.

817   Kim, H.Y., and Davidson, L.A. (2013). Microsurgical Approaches to Isolate Tissues from
818   Xenopus Embryos for Imaging Morphogenesis. Cold Spring Harb Protoc 362–365.

819   Kim, S.W., Fang, X., Ji, H., Paulson, A.F., Daniel, J.M., Ciesiolka, M., van Roy, F., and McCrea,
820   P.D. (2002). Isolation and Characterization of XKaiso, a Transcriptional Repressor That
821   Associates with the Catenin Xp120 ctn in Xenopus laevis. J. Biol. Chem. *277*, 8202–8208.

822   Krneta-Stankic, V., Sabillo, A., and Domingo, C.R. (2010). Temporal and spatial patterning of
823   axial myotome fibers in Xenopus laevis. Dev. Dyn. *239*, 1162–1177.

824   Kunimoto, K., Bayly, R.D., Vladar, E.K., Vonderfecht, T., Gallagher, A.R., and Axelrod, J.D.
825   (2017). Disruption of Core Planar Cell Polarity Signaling Regulates Renal Tubule
826   Morphogenesis but Is Not Cystogenic. Curr. Biol. *27*, 3120-3131.e4.

827   Lefevre, J.G., Chiu, H.S., Combes, A.N., Vanslambrouck, J.M., Ju, A., Hamilton, N.A., and Little,
828   M.H. (2017). Self-organisation after embryonic kidney dissociation is driven via selective
829   adhesion of ureteric epithelial cells. Dev. *144*, 1087–1096.

830   Li, D., Hallett, M. a, Zhu, W., Rubart, M., Liu, Y., Yang, Z., Chen, H., Haneline, L.S., Chan, R.J.,
831   Schwartz, R.J., et al. (2011). Dishevelled-associated activator of morphogenesis 1 (Daam1) is
832   required for heart morphogenesis. Development *138*, 303–315.

833   Li, J.X.H., Tang, V.W., and Brieher, W.M. (2020). Actin protrusions push at apical junctions to
834   maintain E-cadherin adhesion. Proc. Natl. Acad. Sci. U. S. A. *117*, 432–438.

835   Lienkamp, S.S., Liu, K., Karner, C.M., Carroll, T.J., Ronneberger, O., Wallingford, J.B., and
836   Walz, G. (2012). Vertebrate kidney tubules elongate using a planar cell polarity-dependent,
837   rosette-based mechanism of convergent extension. Nat. Genet. *44*, 1382–1387.

838   Liu, W., Sato, A., Khadka, D., Bharti, R., Diaz, H., Runnels, L.W., and Habas, R. (2008).
839   Mechanism of activation of the Formin protein Daam1. Proc. Natl. Acad. Sci. U. S. A. *105*, 210–
840   215.

841   Lu, J., Meng, W., Poy, F., Maiti, S., Goode, B.L., and Eck, M.J. (2007). Structure of the FH2
842   Domain of Daam1: Implications for Formin Regulation of Actin Assembly. J. Mol. Biol. *369*,
843   1258–1269.

844   Marciano, D.K., Brakeman, P.R., Lee, C., Spivak, N., Eastburn, D.J., Bryant, D.M., Iii, G.M.B.,

845 Hofmann, I., Mostov, K.E., Reichardt, L.F., et al. (2011). P120 catenin is required for normal
846 renal tubulogenesis and glomerulogenesis. Development *138*, 2099–2109.

847 McMahon, A.P. (2016). Development of the Mammalian Kidney. Curr. Top. Dev. Biol. 31–64.

848 Mendonsa, A.M., Na, T.Y., and Gumbiner, B.M. (2018). E-cadherin in contact inhibition and
849 cancer. Oncogene *37*, 4769–4780.

850 Miller, R.K., and McCrea, P.D. (2009). Wnt to build a tube: Contributions of Wnt signaling to
851 epithelial tubulogenesis. Dev. Dyn. *239*, NA-NA.

852 Miller, R.K., Gomez de la Torre Canny, S., Jang, C.-W., Cho, K., Ji, H., Wagner, D.S., Jones,
853 E.A., Habas, R., and McCrea, P.D. (2011). Pronephric Tubulogenesis Requires Daam1-
854 Mediated Planar Cell Polarity Signaling. J. Am. Soc. Nephrol. *22*, 1654–1664.

855 Moody, S.A., and Kline, M.J. (1990). Segregation of fate during cleavage of frog (Xenopus
856 laevis) blastomeres. Anat. Embryol. (Berl). *182*, 347–362.

857 Nagy, I.I., Xu, Q., Naillat, F., Ali, N., Miinalainen, I., Samoylenko, A., and Vainio, S.J. (2016).
858 Impairment of Wnt11 function leads to kidney tubular abnormalities and secondary glomerular
859 cystogenesis. BMC Dev. Biol. *16*, 1–14.

860 Nieuwkoop, P.D., and Faber, J. (1994). Normal table of Xenopus laevis (Daudin) : a
861 systematical and chronological survey of the development from the fertilized egg till the end of
862 metamorphosis (New York: Garland Publishing, Inc.).

863 Nishimura, T., Honda, H., and Takeichi, M. (2012). Planar cell polarity links axes of spatial
864 dynamics in neural-tube closure. Cell *149*, 1084–1097.

865 Nishimura, T., Ito, S., Saito, H., Hiver, S., Shigetomi, K., Ikenouchi, J., and Takeichi, M. (2016).
866 DAAM1 stabilizes epithelial junctions by restraining WAVE complex-dependent lateral
867 membrane motility. J. Cell Biol. *215*, 559–573.

868 Nworu, C.U., Krieg, P.A., and Gregorio, C.C. (2014). Preparation of developing Xenopus muscle
869 for sarcomeric protein localization by high-resolution imaging. Methods *66*, 370–379.

870 O'Brien, L.L., Combes, A.N., Short, K.M., Lindström, N.O., Whitney, P.H., Cullen-McEwen, L.A.,
871 Ju, A., Abdelhalim, A., Michos, O., Bertram, J.F., et al. (2018). Wnt11 directs nephron progenitor
872 polarity and motile behavior ultimately determining nephron endowment. Elife *7*, 1–25.

873 Saxen, L. (1987). Organogenesis of the Kidney (Cambridge University Press).

874 Shindo, A., and Wallingford, J.B. (2014). PCP and septins compartmentalize cortical actomyosin
875 to direct collective cell movement. Science *343*, 649–652.

876 Sive, H.L., Grainger, R.M., and Harland, R.M. (2000). Early development of Xenopus laevis : a
877 laboratory manual (Cold Spring Harbor Press, Cold Spring Harbor, NY, USA: Cold Spring
878 Harbor Laboratory Press).

879 Strickland, L., Von Dassow, G., Ellenberg, J., Foe, V., Lenart, P., and Burgess, D. (2004). Light
880 microscopy of echinoderm embryos. Methods Cell Biol. *2004*, 371–409.

881 Tada, M., and Heisenberg, C.P. (2012). Convergent extension: using collective cell migration
882 and cell intercalation to shape embryos. Development *139*, 3897–3904.

883 Takeichi, M. (2014). Dynamic contacts: Rearranging adherens junctions to drive epithelial
884 remodelling. Nat. Rev. Mol. Cell Biol. *15*, 397–410.

885 Venegas-FERRÍN, M., Sudou, N., Taira, M., and Del Pino, E.M. (2010). Comparison of Lim1
886 expression in embryos of frogs with different modes of reproduction. Int. J. Dev. Biol. *54*, 195–
887 202.

888   Vestweber, D., Kemler, R., and Ekblom, P. (1985). Cell-adhesion molecule uvomorulin during
889   kidney development. Dev. Biol. *112*, 213–221.

890   Vize, P.D., Carroll, T.J., and Wallingford, J.B. (2003). Induction, Development, and Physiology
891   of the Pronephric Tubules. In The Kidney, P.D. Vize, A.S. Woolf, and J.B.L. Bard, eds. (San
892   Diego: Elsevier), pp. 19–50.

893   Williams, E., Villar-Prados, A., Bowser, J., Broaddus, R., and Gladden, A.B. (2017). Loss of
894   polarity alters proliferation and differentiation in low-grade endometrial cancers by disrupting
895   Notch signaling. PLoS One *12*, e0189081.

896   Yamashita, M., Higashi, T., Suetsugu, S., Sato, Y., Ikeda, T., Shirakawa, R., Kita, T., Takenawa,
897   T., Horiuchi, H., Fukai, S., et al. (2007). Crystal structure of human DAAM1 formin homology 2
898   domain. Genes Cells *12*, 1255–1265.

899   Yap, A.S., Gomez, G.A., and Parton, R.G. (2015). Adherens Junctions Revisualized: Organizing
900   Cadherins as Nanoassemblies. Dev. Cell *35*, 12–20.

901
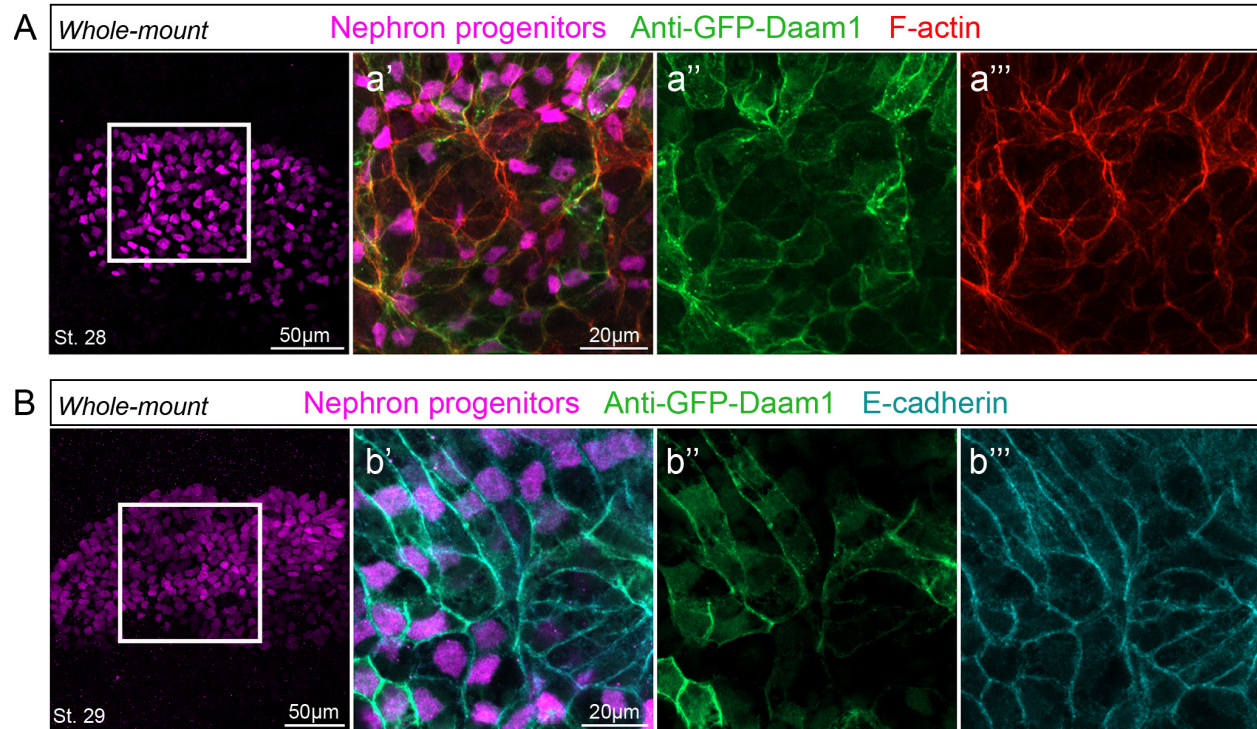
Figure 1. Daam1 co-localizes with junctional F-actin and E-cadherin during early nephron development
Confocal maximum image projections of whole-mount immunostaining of *Xenopus* nephric primordium labeled by Lhx1(magenta) and GFP to visualize Daam1 (green) in conjunction with, (A) Phalloidin staining to visualize F-actin (red) or (B) E-cadherin (cyan). a'-a''' and b'-b''' represent close-up images of white boxes.
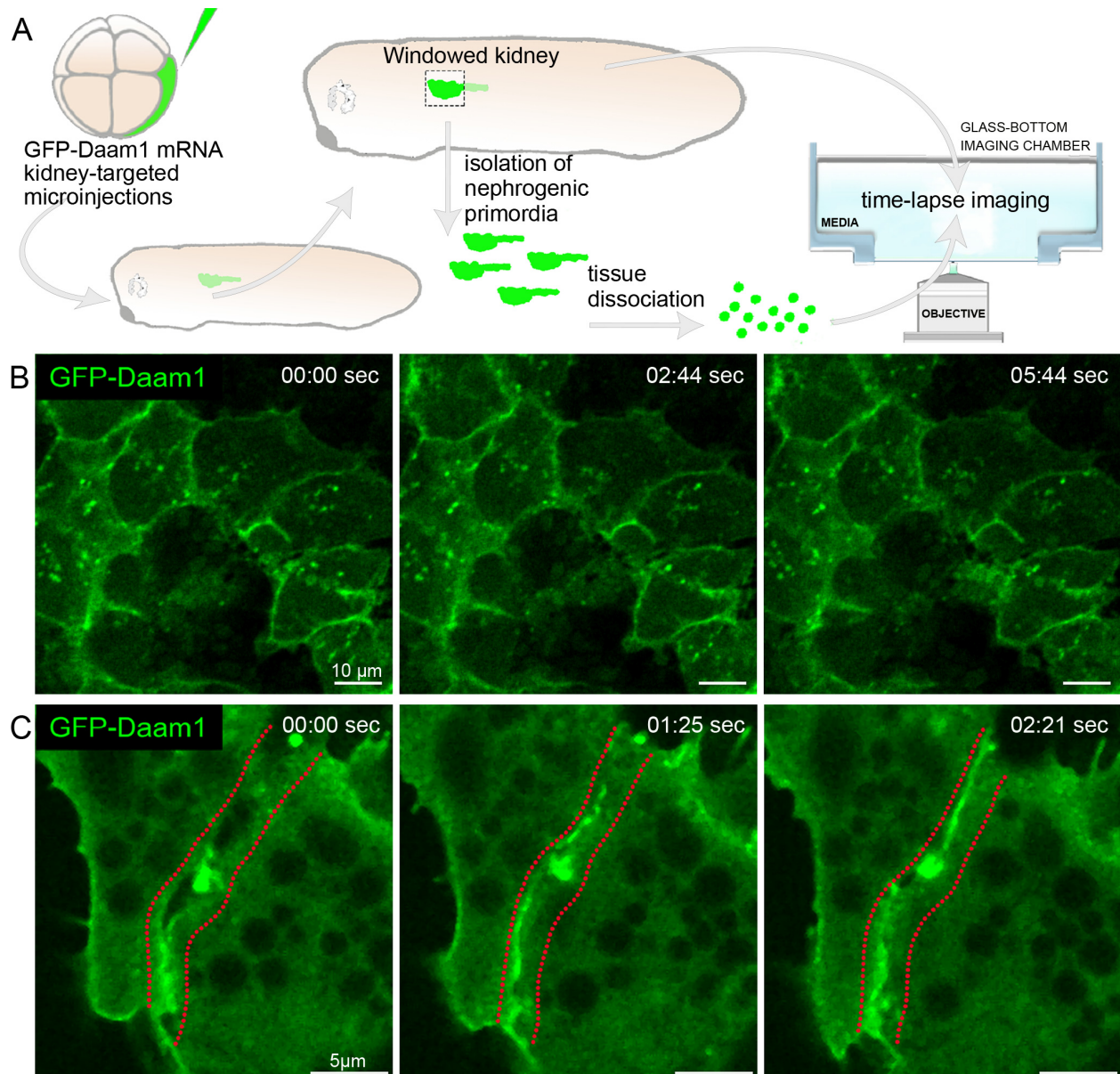
Figure 2. Daam1 localizes to newly formed cell-cell contacts

(A) Schematic illustration showing steps involved in preparation of "windowed kidney" embryos and primary cultures expressing GFP-Daam1. Please note that for clarity of illustration the 8-cell GFP-Daam1 injected *Xenopus* blastomere is fate-mapped strictly to the nephric primordium and that blastomere also contributes to epidermis, ventral and dorsal somites, hidgut, proctodeum and trunk neural crest cells (DeLay et al., 2016; Moody and Kline, 1990).

(B) Time-lapse imaging montage of the nephric primordium expressing GFP-Daam1 in "windowed kidney" embryos. Elapsed time is indicated at the top in seconds; see Video S1.

(C) Time-lapse imaging montage shows cells isolated from a developing nephron expressing GFP-Daam1 mRNA adhering with each other. Elapsed time is indicated at the top in seconds. The border arising between two cells is delineated by the red dotted line; see Video S2.
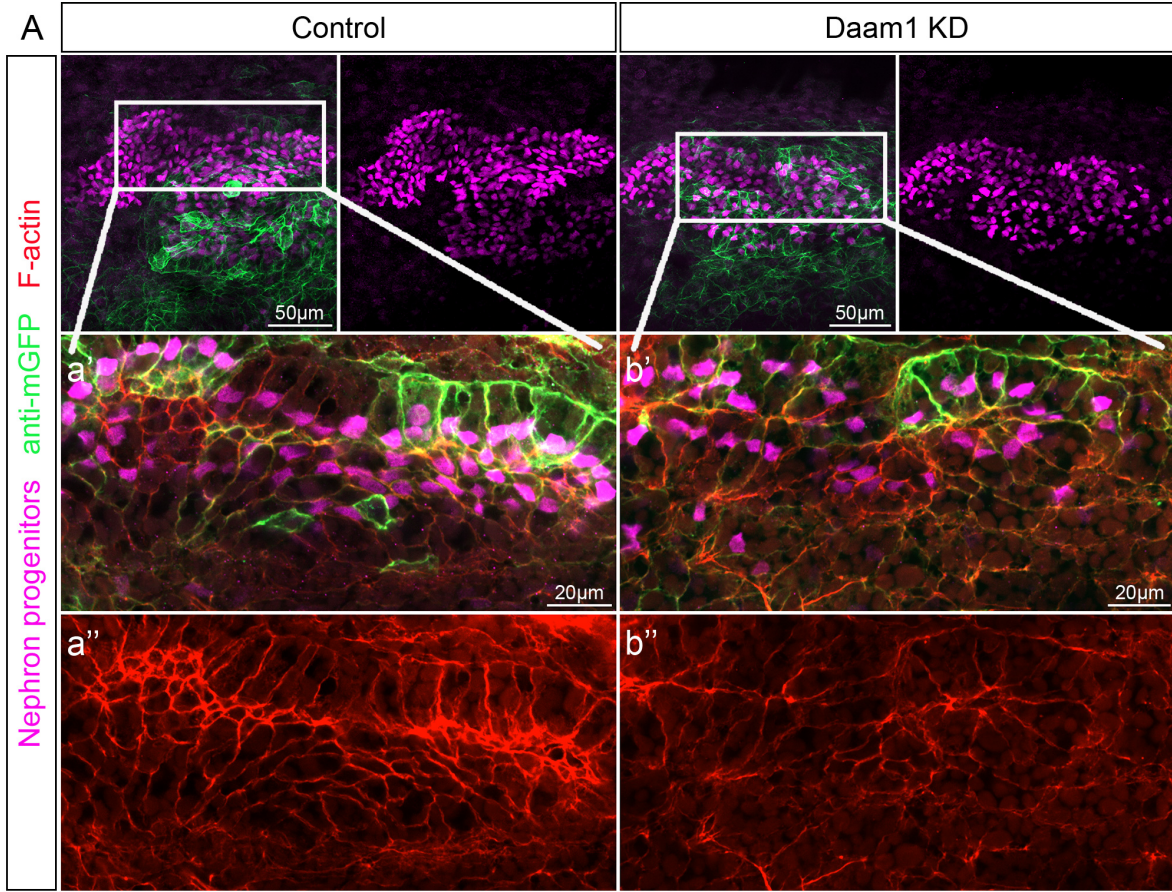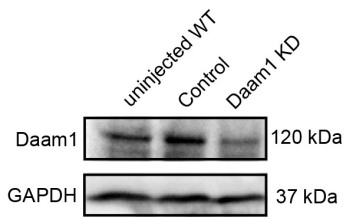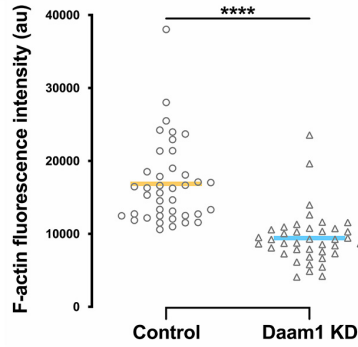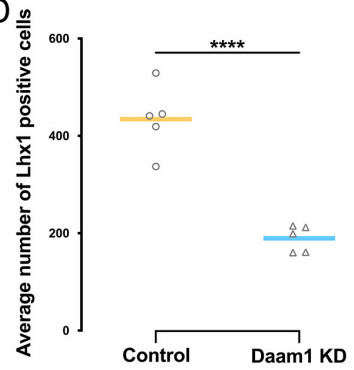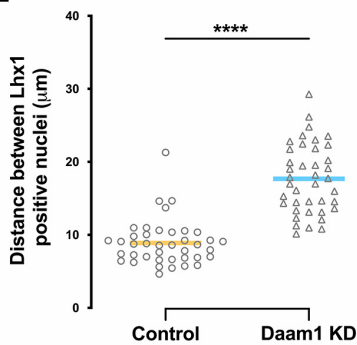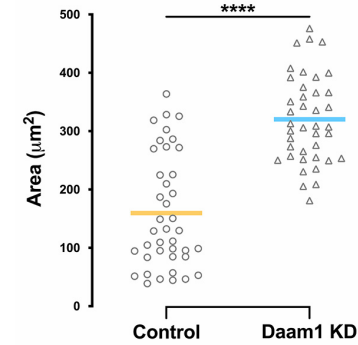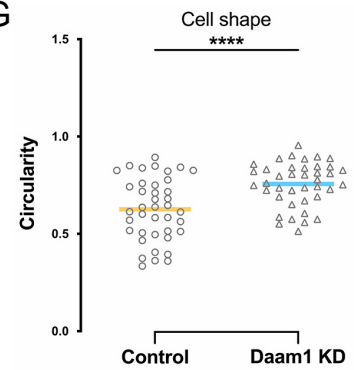
Figure 3. Effects of Daam1 depletion on the nephrogenic primordium

(A) Maximum projection confocal images of F-actin expression (red) in nephric primordium (magenta) in Control and Daam1 knockdown embryos. a-a'' and b'-b'' represent close-up images of the corresponding regions in white boxes; see Videos S3 and S4.

(B) Western blot showing Daam1 and GAPDH (control) protein levels for uninjected wild type (WT) and Control (Standard morpholino) and Daam1 KD (Daam1 morpholino) injected embryos.

(C) The graph showing the relative fluorescence intensity levels of junctional F-actin in the nephric primordia of Control and Daam1 KD embryos. $N_{Control}$=40 junctions on 2 embryos and $N_{Daam1\ KD}$=40 junctions on 2 embryos. ****P < 0.0001 analyzed by unpaired t-test.

(D-G) Morphometric analyses of Control and Daam1-depleted nephric primordia. The thick bars represent the mean, ****P < 0.0001 analyzed by unpaired t-test, (E-G) $N_{Control}$=40 junctions on 2 embryos and $N_{Daam1\ KD}$=40 junctions on 2 embryos. Graphs showing comparison between Control and Daam1-depleted nephric primordia of,

(D) the average number of Lhx1-positive nephron progenitors where $N_{Control}$=5 embryos and $N_{Daam1KD}$=5 embryos,

(E) the relative distance between nearest neighbors of Lhx1-positive nuclei,

(F) the relative cell area and

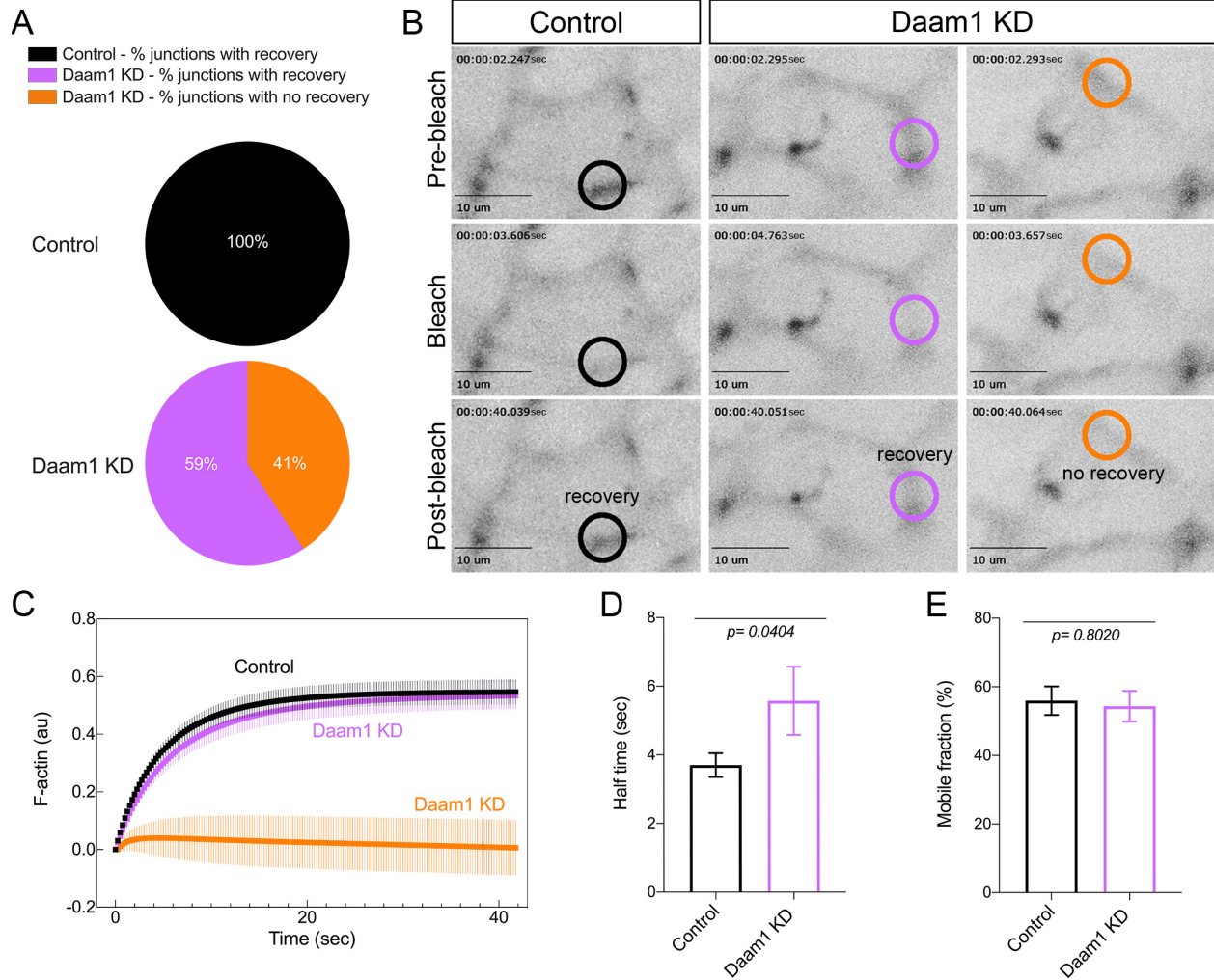(G) the relative circularity, where 1 represents the perfect circle.

Figure 4. Daam1 regulates assembly of junctional F-actin in developing nephron

F-actin dynamics at cell-cell junctions of Control and Daam1-depleted developing nephrons expressing mCherry-Utrophin were assessed using FRAP.

(A) Percentage of junctions showing recovery of fluorescence after bleaching in Control (black, N_{total}=27 junctions, 1-5 junctions/embryo) and Daam1 KD (purple and orange, N_{total}=27 junctions, 1-5 junctions/embryo) nephrons.

(B) Typical time-lapse images of Control and Daam1-depleted cell junctions before and after photobleaching. In each image, the bleached region is highlighted with a circle (black - Control junction showing recovery, purple - Daam1 KD junction showing recovery and orange - Daam1 KD junction showing no-recovery of fluorescence after photobleaching).

(C) Graph shows average recovery curves obtained from individual best-fit plots for Control (black), Daam1 KD junctions with (purple) and without (orange) recovery of fluorescence after photobleaching.

(D-E) Bar graphs comparing Control and Daam1 KD profiles calculated from individual best-fit curves for Control (black) and Daam1 KD junctions with recovery of fluorescence after photobleaching (purple). Data represent the mean ± S.E. from three independent experiments. P-values were analyzed by unpaired t-test.

(D) Bar graph of the relative half-times for F-actin.

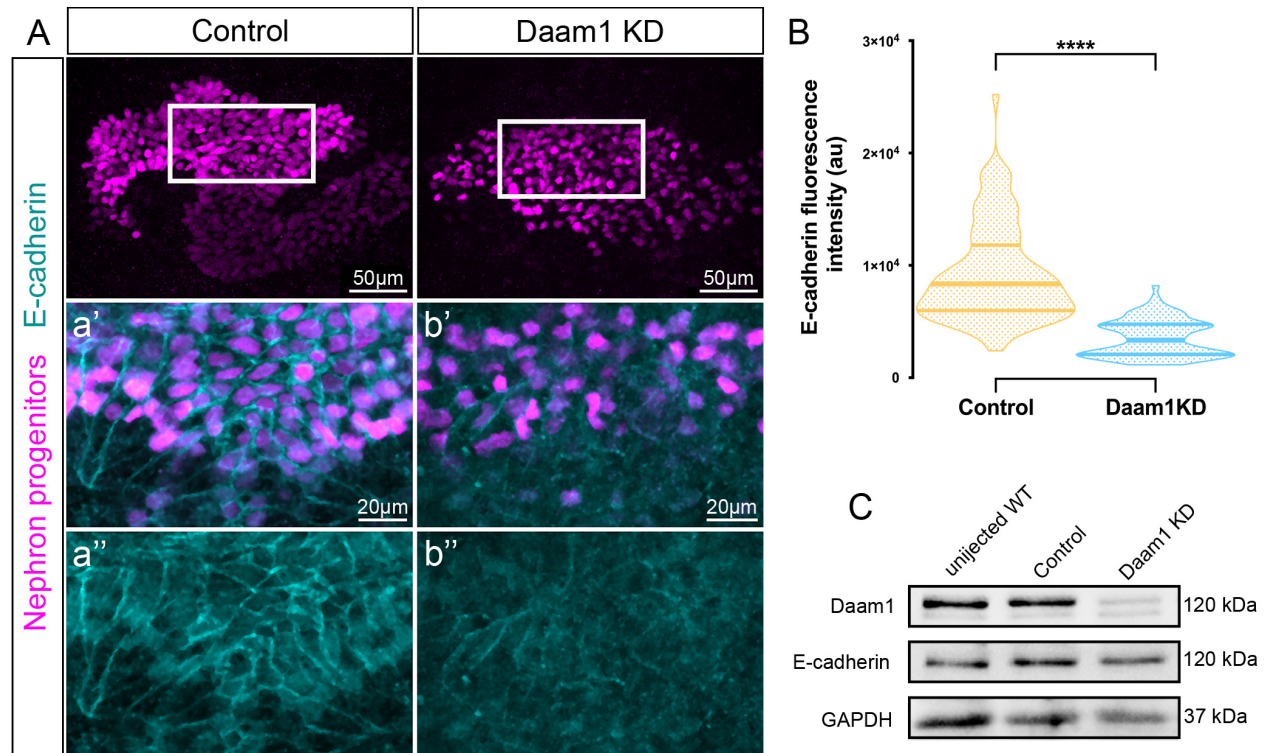(E) Bar graph of the relative mobile fraction for F-actin.

Figure 5. Daam1 promotes localization of junctional E-cadherin

(A) Maximum projection confocal images of E-cadherin expression (cyan) in nephric primordium (magenta) in Control and Daam1 KD embryos a-a' and b-b' represent the close-up images of corresponding regions in white boxes.

(B) Violin plots depicting the relative fluorescence intensity of junctional E-cadherin in the nephric primordia of Control (orange) and Daam1 KD (blue). $N_{Control}$=88 junctions on 4 embryos and $N_{Daam1\ KD}$=84 junctions on 4 embryos. Center-lines represents median; Limits show 1st and 3rd quartile. ****P<0.0001 analyzed by unpaired t-test.

(C) Western blot showing Daam1, E-cadherin and GAPDH (control) protein levels in uninjected wild type (WT) and Control (Standard morpholino) and Daam1 KD (Daam1 morpholino) injected embryos.

Figure 6. E-cadherin localization to cell-cell junctions is mediated by FH2 domain of Daam1

(A) Maximum projection confocal images showing E-cadherin staining (cyan) in nephric primordium (magenta) expressing GFP-Daam1 or GFP-Daam1 FH2 mutant mRNA. a-a' and b-b' represent close-up images of corresponding regions in white boxes.

(B) Violin plots depicting the relative fluorescence intensity of junctional E-cadherin in the nephric primordia expressing GFP-Daam1 (orange) and GFP-Daam1 FH2 mutant (blue) mRNA. N_{Daam1}=60 junctions on 3 embryos and $N_{Daam1FH2mutant}$=55 junctions on 3 embryos. Center-lines represents median; Limits show 1st and 3rd quartile. ***P<0.0002 analyzed by unpaired t-test.

(C) Western blot showing the exogenous and endogenous protein levels of Daam1 in uninjected wild type (WT) embryos, embryos injected with 1 ng of GFP-Daam1 mRNA and 1ng GFP-Daam1 FH2 mutant mRNA. The non-specific band confirms equal loading.
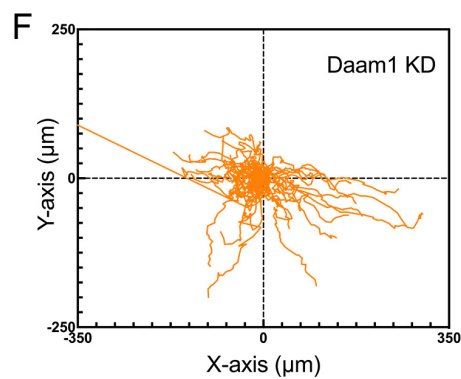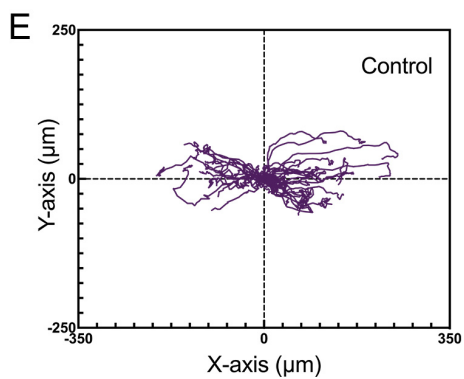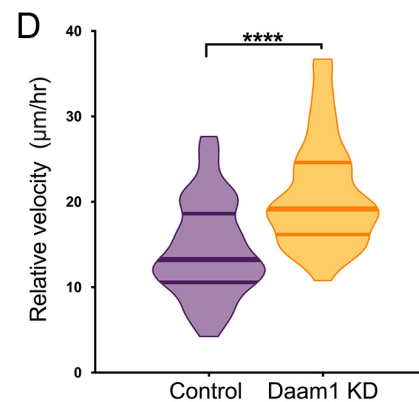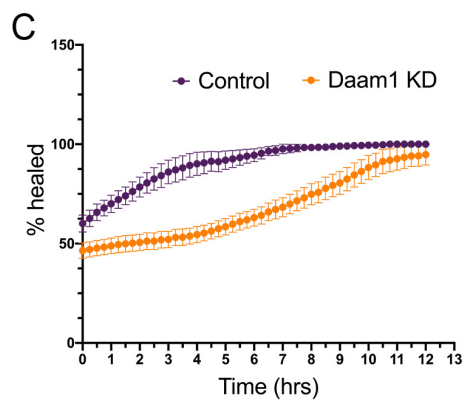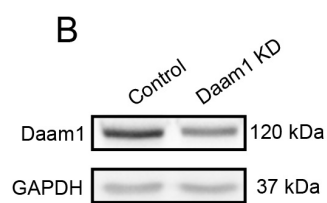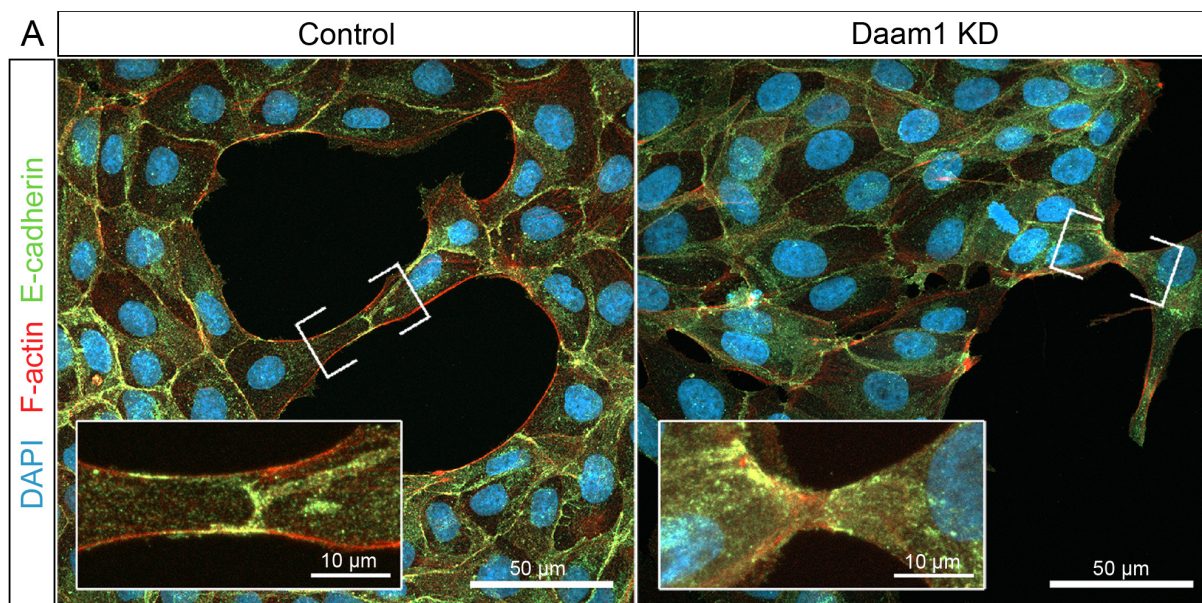
Figure 7. Daam1- depleted MDCK cells display compromised localization of E-cadherin at cell-cell contacts and impaired cohesion during collective movement

(A) E-cadherin (green), F-actin (red) and DAPI (blue) in subconfluent the MDCK Control and shDaam1 knockdown cells. E-cadherin localization in the nascent cell-cell contacts (marked by white brackets and shown enlarged in corresponding white boxes) is impaired in shDaam1- deficient cells.

(B) Western blot analysis of Daam1 and GAPDH protein levels in the MDCK Control and shDaam1 knockdown cells.

(C-F) Summary of the wound-healing experiments for the MDCK Control and Daam1 KD cells, see Video S7.

(C) Daam1 depletion impairs wound closure. The graph represents the percent of the wound surface area over time for Control (purple) and Daam1 KD (orange) cells. Error bars indicate S.E. of the mean on 4 assays.

(D-F) Manually tracking migration paths of single-cells during the wound closure demonstrates that Daam1 organizes collective movement of the MDCK epithelial monolayers by modulating the speed and directionality of individual cells. Depletion of Daam1 results in increased velocity and random migration. $N_{Control}$=52 cells from 4 assays and $N_{Daam1 KD}$=42 cells tracked from 4 assays. Cells were tracked in 15 minutes increments for 12 hours.

(D) Violin plots represent migration velocity calculated from tracking traveled distances of single cells for Control and Daam1 KD cells. Center-lines represents median; Limits show 1st and 3rd quartile. ***P<0.0001 analyzed by unpaired t-test.

(E) Wind-rose plot showing migration tracks of individual Control cells.

(F) Wind-rose plot showing migration tracks of Daam1 KD cells.